

**Effects of ZrO<sub>2</sub> on thermal stability and crystallization of K<sub>2</sub>O-Al<sub>2</sub>O<sub>3</sub>-SiO<sub>2</sub> glasses**

DENG, Wei, CHRISTOPOULOU, Georgia, MODARRESIFAR, Farid, JONES, Alan and BINGHAM, Paul <<http://orcid.org/0000-0001-6017-0798>>

Available from Sheffield Hallam University Research Archive (SHURA) at:

<https://shura.shu.ac.uk/29218/>

---

This document is the Accepted Version [AM]

**Citation:**

DENG, Wei, CHRISTOPOULOU, Georgia, MODARRESIFAR, Farid, JONES, Alan and BINGHAM, Paul (2021). Effects of ZrO<sub>2</sub> on thermal stability and crystallization of K<sub>2</sub>O-Al<sub>2</sub>O<sub>3</sub>-SiO<sub>2</sub> glasses. *European Journal of Glass Science and Technology Part B Physics and Chemistry of Glasses*, 62 (5), 137-148. [Article]

---

**Copyright and re-use policy**

See <http://shura.shu.ac.uk/information.html>

# Effects of ZrO<sub>2</sub> on thermal stability and crystallization of K<sub>2</sub>O-Al<sub>2</sub>O<sub>3</sub>-SiO<sub>2</sub> glasses

W. Deng <sup>a, 1</sup>, G. Christopoulou <sup>a</sup>, F. Modarresifar <sup>a, b</sup>, A. H. Jones <sup>a</sup>, and P. A. Bingham <sup>a, 1</sup>

<sup>a</sup> Materials and Engineering Research Institute, College of Business, Technology and Engineering, Sheffield Hallam University, City Campus, Howard Street, Sheffield S1 1WB, UK.

<sup>b</sup> Morgan Advanced Materials, Thermal Ceramics UK, Tebay Road, Bromborough CH62 3PH, UK.

## Abstract

The thermal stability and crystallization behaviour of two refractory glass-forming compositions in the K<sub>2</sub>O-Al<sub>2</sub>O<sub>3</sub>-SiO<sub>2</sub> ternary system were studied without ZrO<sub>2</sub> additions (samples KAS1 and KAS2, with compositions on the tie-lines from KAlSiO<sub>4</sub> to Al<sub>2</sub>O<sub>3</sub> and from KAlSi<sub>2</sub>O<sub>6</sub> to Al<sub>2</sub>O<sub>3</sub>, respectively) and with ZrO<sub>2</sub> additions (samples KAS1-Z and KAS2-Z). X-ray diffraction (XRD) was used to determine the crystalline phases formed during the heat treatment of the glasses. All as-prepared glasses were amorphous, except KAS2, with a weak SiO<sub>2</sub> phase attributed to imperfect melting of starting materials, which disappeared upon heat treatment. Full crystallization of kalsilite (KAlSiO<sub>4</sub>) was observed in sample KAS1 after only 5 minutes' heat treatment at 1250°C; for sample KAS2, a minor phase transformation from  $\gamma$ -Al<sub>2</sub>O<sub>3</sub> to  $\alpha$ -Al<sub>2</sub>O<sub>3</sub> was observed after 10 minutes' heat treatment at 1250°C;

---

<sup>1</sup> Corresponding authors, email [wei.deng@shu.ac.uk](mailto:wei.deng@shu.ac.uk); [p.a.bingham@shu.ac.uk](mailto:p.a.bingham@shu.ac.uk)

the relict SiO<sub>2</sub> phase disappeared and the major phase leucite (KAlSi<sub>2</sub>O<sub>6</sub>) began to form after 30 minutes in sample KAS2. Upon addition of ZrO<sub>2</sub> (sample KAS2-Z) the transformation from  $\gamma$ -Al<sub>2</sub>O<sub>3</sub> to  $\alpha$ -Al<sub>2</sub>O<sub>3</sub> was delayed and observed after 30 minutes' heat treatment at 1250°C. Meanwhile, the promotion of kalsilite and leucite crystallization was observed in samples KAS1-Z and KAS2-Z, respectively. Differential scanning calorimetry (DSC) was used to determine characteristic temperatures and crystallization activation energies ( $E_a$ ) for each glass. However, there was no clear correlation between crystallization tendency (glass-forming ability) and  $E_a$  for these glasses, which exhibit high crystallization tendency. Multiple glass stability parameters (Hrubý  $K_H$ , Weinberg  $K_W$ , Lu & Liu  $K_{LL}$ ) were calculated based on characteristic temperatures and a further criterion (Hu  $k$ ) was calculated, based on  $E_a$ . Promotion of the major phase (kalsilite and leucite) crystallization by the addition of ZrO<sub>2</sub> was confirmed through these criteria.

**Keywords:** glass, glass-ceramic, crystallization, glass stability, glass structure, ZrO<sub>2</sub>

## 1. Introduction

### 1.1 Background

The ternary oxide system K<sub>2</sub>O-Al<sub>2</sub>O<sub>3</sub>-SiO<sub>2</sub> is important for multiple glass, ceramic, refractory and glass-ceramic applications [1–4]. Common crystalline phases forming within this system include potassium feldspar (K<sub>2</sub>O·Al<sub>2</sub>O<sub>3</sub>·6SiO<sub>2</sub>), leucite (K<sub>2</sub>O·Al<sub>2</sub>O<sub>3</sub>·4SiO<sub>2</sub>), kalsilite (K<sub>2</sub>O·Al<sub>2</sub>O<sub>3</sub>·2SiO<sub>2</sub>), mullite (3Al<sub>2</sub>O<sub>3</sub>·2SiO<sub>2</sub>), and quartz

(SiO<sub>2</sub>). Understanding and manipulation of phase relations and transformations within this system have always been important as they directly impact upon applications including high temperature refractories (in the form of blocks or fibres) and electronic, optical and dental replacement materials.

In respect of refractory applications, mullite ceramics are well known in the Al<sub>2</sub>O<sub>3</sub>-SiO<sub>2</sub> system, and mullite is also a primary phase occurring in the K<sub>2</sub>O-Al<sub>2</sub>O<sub>3</sub>-SiO<sub>2</sub> system. Polycrystalline mullite retains >90% of its room-temperature strength to 1500°C and displays very high creep and thermal shock resistance [5]. Mullite is the only stable binary compound under atmospheric conditions in the Al<sub>2</sub>O<sub>3</sub>-SiO<sub>2</sub> system [6]. Impurity oxides in this system, such as alkali oxides, alkaline earth oxides, titanium and iron oxides, have also attracted attention. Some of these impurities can form solid solution in the mullite phase, but most react with Al<sub>2</sub>O<sub>3</sub> or SiO<sub>2</sub> to form eutectics that not only increase the amount of glassy phase in refractories, but also affect the liquid phase high temperature performance. Potassium, the addition of which forms the K<sub>2</sub>O-Al<sub>2</sub>O<sub>3</sub>-SiO<sub>2</sub> system, is also important: for example, in Al<sub>2</sub>O<sub>3</sub>-SiO<sub>2</sub> refractories, alkalis react with the glassy matrix and then with the mullite grains [6–8]. The potassium-bearing compounds formed in these reactions can, in some cases, cause cracking due to volume expansion caused by the precipitation of phases such as feldspar, leucite, kalsilite or kaliophilite, leading to premature failure of these refractories. Scudeller *et al.* [9] considered a refractory with 50 wt% Al<sub>2</sub>O<sub>3</sub> and 50 wt% SiO<sub>2</sub> that was attacked by potassium-bearing vapour at high temperature. The tie-line of the SiO<sub>2</sub>-Al<sub>2</sub>O<sub>3</sub> midpoint and K<sub>2</sub>O in the K<sub>2</sub>O-Al<sub>2</sub>O<sub>3</sub>-SiO<sub>2</sub> phase diagram

illustrates the compositional change of the refractory. As shown in Figure 1, this line passes through 5 compatibility triangles and a large liquid-phase region with increasing  $K_2O$  content, which illustrates the complex equilibrium relationships between the different phases including mullite, feldspar, leucite, kalsilite and liquid.

In terms of other applications, conventional fibre high-temperature thermal insulation materials include refractory ceramic fibre (RCF) materials, and these are now classified as Category 1A or 1B by the World Health Organization (definite and possible human carcinogens, respectively) [10–12]. Consequently, alternative refractory fibre materials, including materials based on the  $K_2O-Al_2O_3-SiO_2$  system, have recently been developed [13]. The  $K_2O-Al_2O_3-SiO_2$  ternary system has been widely used in ceramic research and is fundamentally important in multiple glass, ceramic and glass ceramic applications. The  $K_2O-Al_2O_3-SiO_2$  ternary system was experimentally studied by Schairer and Bowen [14] and a partial phase diagram of this system was revised and redrawn by Osborn and Muan [15] (Figure 2). Kingery *et al.* [1] also presented a partial isothermal section of this system at 1200°C (Figure 3).

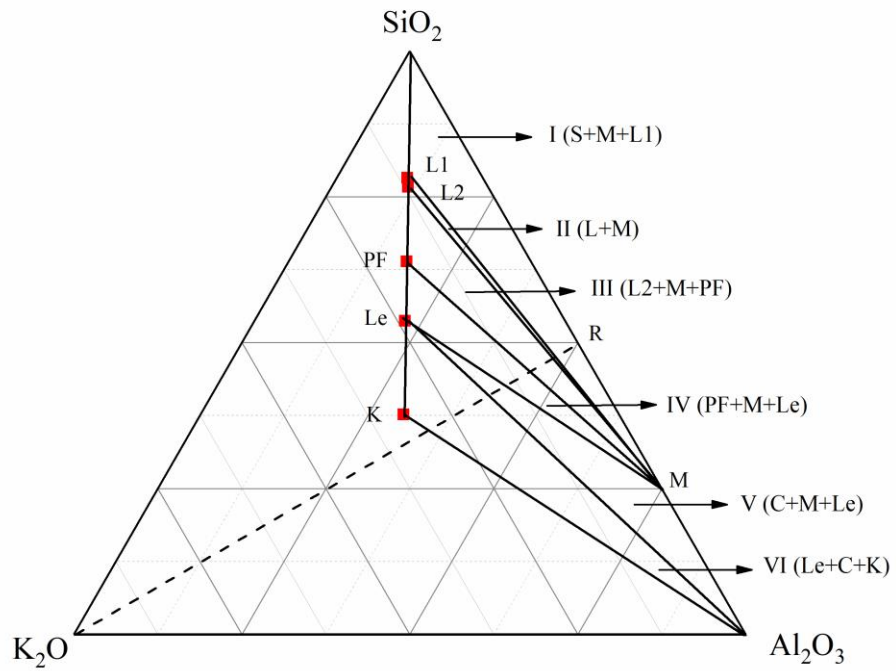


**Figure 1.** Refractory compositions (on the K<sub>2</sub>O-R dotted line) from Scudeller *et al.* [9]

(S=Silica; M= Mullite; L, L2, L3=Liquid; PF=Potash Feldspar; Le=Leucite; C=Corundum; K=Kaliophilite.)

Reproduced with permission of the Journal of the American Ceramic Society, license # 4860380913652.

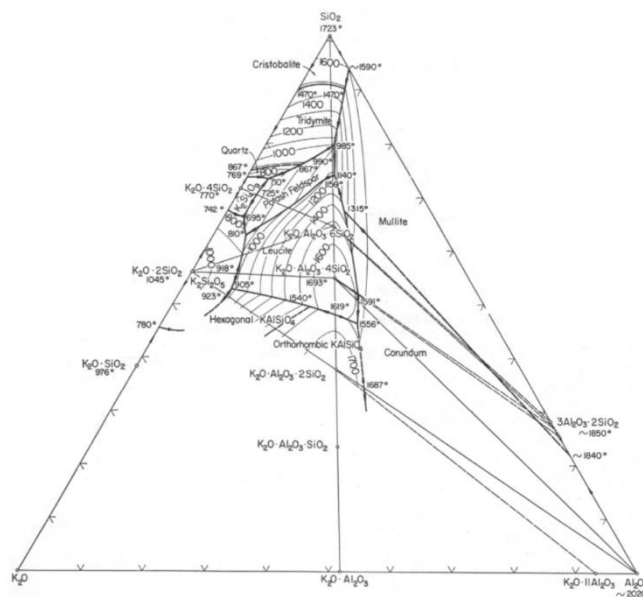


**Figure 2.** K<sub>2</sub>O-Al<sub>2</sub>O<sub>3</sub>-SiO<sub>2</sub> ternary phase diagram experimentally studied by Schairer and Bowen [14] and revised

and redrawn by Osborn and Muan [15] Reproduced from phase equilibria diagrams online database (NIST standard Reference Database 31, Figure 00407), with permission of The American Ceramic Society.

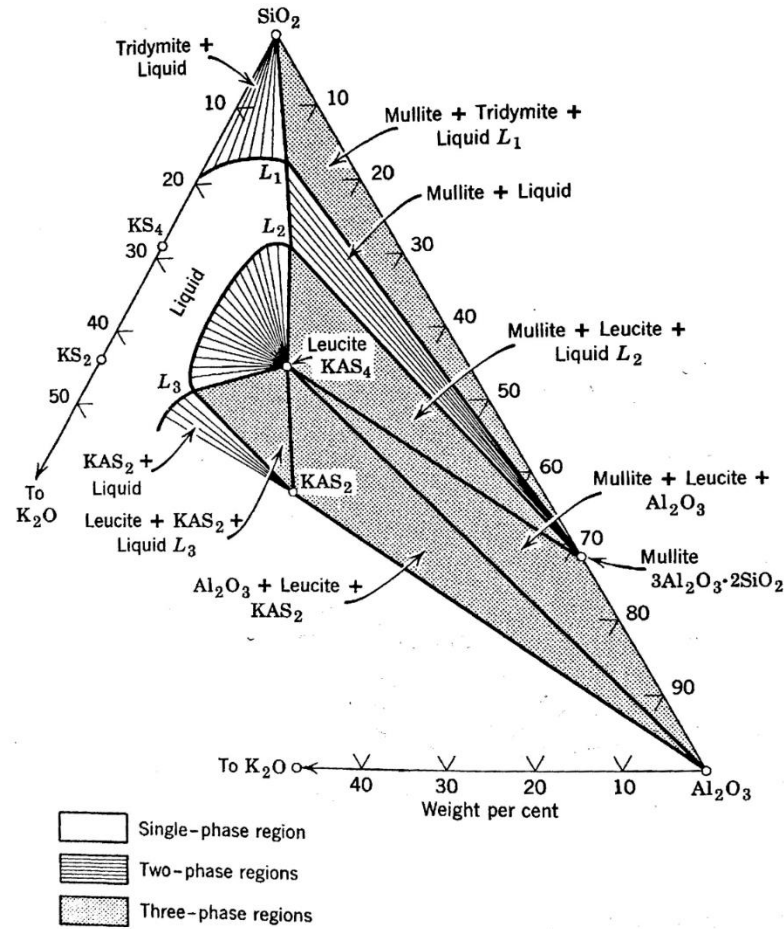


**Figure 3.** Isothermal section in the  $K_2O-Al_2O_3-SiO_2$  diagram at  $1200^\circ C$  from Kingery *et al.* [1] (Note:  $KAS_2$  is the composition  $K_2O \cdot Al_2O_3 \cdot 2SiO_2$ ). Reproduced with permission of Wiley publishers, license # 4860380753214.

For decades, several different processes and applications have utilized different compositions within this ternary system [9,16–19]. However, the large low-temperature liquid areas in the  $K_2O$ ,  $Al_2O_3$  and  $K_2O \cdot 2SiO_2$  triangles within the system remain relatively unexplored. With the development of new materials in the form of glass-ceramics and fibres [4,20–23] this compositional area has become more technologically interesting. Yazhenskikh *et al.* [24] thermodynamically modelled the  $K_2O-Al_2O_3-SiO_2$  ternary system and produced a phase diagram showing the

calculated liquidus surfaces and binary / ternary invariant points. Their modelled phase diagram closely corroborates the available experimental data and provides useful predictions for the experimentally unstudied parts, especially the high-K<sub>2</sub>O compositional regions. The eutectic lines of K<sub>2</sub>SiO<sub>3</sub>-KAlSiO<sub>4</sub> and KAlSiO<sub>4</sub>-K<sub>2</sub>Al<sub>12</sub>O<sub>19</sub> were indicated, and a solid solution based on KAlO<sub>2</sub> predicted to coexist in equilibrium with a liquid phase in the K<sub>2</sub>O-rich corner. However, information for the region below the Al<sub>2</sub>O<sub>3</sub>- K<sub>2</sub>O·2SiO<sub>2</sub> tie-line was not presented and thus large areas of the phase diagram still remain unexplored.

Zirconium oxide, ZrO<sub>2</sub>, is well-known in glass-ceramics as a nucleating agent, which is added to the glass to induce crystallization for glass ceramic preparation. As a heterogeneous nucleating agent ZrO<sub>2</sub>, in particular, has been used as a nucleating agent for crystallization of β-quartz or β-spodumene solid solutions in the SiO<sub>2</sub>-Al<sub>2</sub>O<sub>3</sub>-Li<sub>2</sub>O and SiO<sub>2</sub>-Al<sub>2</sub>O<sub>3</sub>-MgO glass systems by microphase separation processes, according to Beall *et al.* [25]. Apart from its effectiveness as a nucleating agent, ZrO<sub>2</sub> has also proven useful in the development of polycrystalline glass-ceramics for technical applications and in medicine and dentistry. Zirconia typically increases the viscosity of oxide glass melts, and melting of glass batches containing zirconium-bearing raw materials (e.g. zircon or zircon sand) usually require increased melting temperatures and times to provide a homogeneous melt. Thus, corrosion of refractory materials in the glass melter may be more pronounced [26].

For the role of ZrO<sub>2</sub> in glass structure, classical theory [27] indicates that Zr<sup>4+</sup> induces crystallization in the glass matrix and reduces the crystallization activation

energy by providing low-energy sites. Farges *et al.* [28] presented EXAFS studies of  $Zr^{4+}$  coordination in selected silicate and aluminosilicate glasses: in all glasses,  $Zr^{4+}$  is mainly 6-coordinated by oxygen. Small amounts of  $Zr^{4+}$  were also found to occur in 8-coordinated sites in the most polymerized albite ( $NaAlSi_3O_8$ ) composition glasses. Further possible structural models suggested  $ZrO_6$  octahedra with four bridging and two non-bridging oxygens [28]. The intermediate role of 6-coordinated  $Zr^{4+}$  in silicate glasses is reflected in its cation field strength and single-oxide bond strength [29].

Recent research by Ficheux *et al.* [30] illustrated the influence of Zr on cation mobilities in silicate and aluminosilicate melts. Through their XANES study,  $Zr^{4+}$  was determined to exist in six-fold coordinated sites which are preferentially charge compensated by  $Na^+$ , which has an initial structural role as a network modifier associated with  $Q^3$  (Si) sites in  $Na_2O$ - $CaO$ - $Al_2O_3$ - $SiO_2$  melts. This modification, upon addition of  $Zr^{4+}$ , generates lower bond strengths between sodium and other cations in the melt, which strongly suggests that the sodium mobility is enhanced by the presence of  $Zr^{4+}$ , despite the viscosity increase due to the addition of  $ZrO_2$  [30]. Through the diffusion coefficients of network formers calculated from measured viscosities by the Eyring relation by Ficheux *et al.* [30] it was shown that  $Zr^{4+}$  not only provides low energy sites for crystallization, it also increases the network modifier ionic diffusivity (which also generally enhances crystallization) as well as increasing high temperature viscosity.

## 1.2 Current Research

Previously we studied nonisothermal crystallization kinetics and stability of leucite ( $\text{K}_2\text{O}\cdot\text{Al}_2\text{O}_3\cdot 4\text{SiO}_2$ ) and kalsilite ( $\text{K}_2\text{O}\cdot\text{Al}_2\text{O}_3\cdot 2\text{SiO}_2$ ) from glasses in the  $\text{K}_2\text{O}\text{-Al}_2\text{O}_3\text{-SiO}_2$  system [16], showing that kalsilite is an unstable phase which behaves as an intermediate precursor to leucite. Kalsilite loses potassium upon prolonged heat treatment with formation of leucite from stoichiometric kalsilite, accompanied by the formation of potassium-doped  $\beta\text{-Al}_2\text{O}_3$ . We also demonstrated that pure leucite ( $\text{K}_2\text{O}\cdot\text{Al}_2\text{O}_3\cdot 4\text{SiO}_2$ ) can be formed with more favourable crystallization kinetics if the starting compositions are off-stoichiometric. In the present work, we build on our previous study to consider the effects of  $\text{ZrO}_2$  additions on thermal stability and crystallization behaviour of two selected glasses in the  $\text{K}_2\text{O}\text{-Al}_2\text{O}_3\text{-SiO}_2$  system (Figure 4), each with and without  $\text{ZrO}_2$  additions. These compositions were selected so as to present relevance to the compositions studied in our previous work [16], whilst offering new compositional information to expand the pool of knowledge on new and technologically-interesting compositions in this system. Differential thermal analysis was used to determine thermal properties. Glass compositions, crystalline phase relations and phase transitions upon heating were studied by X-ray fluorescence (XRF) and X-ray diffraction (XRD). Glass stability and crystallization activation energies were determined via application of the Kissinger equation [31] and a series of glass thermal stability equations to the thermal analysis data.

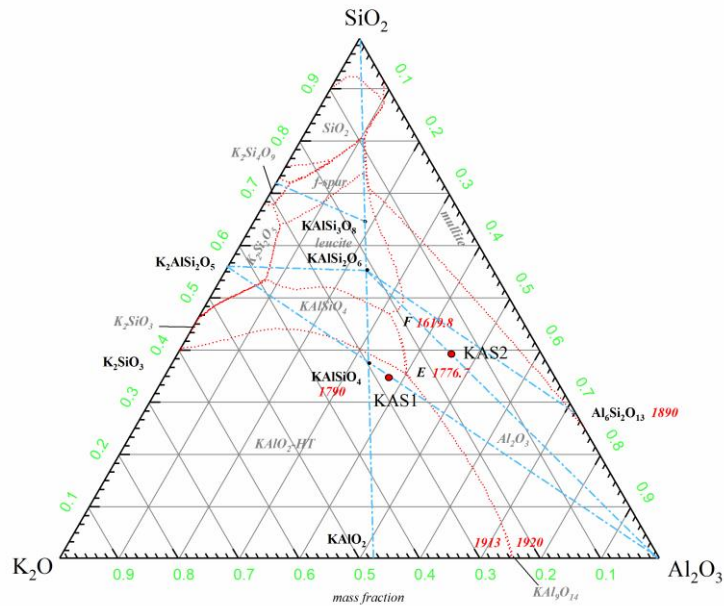


**Figure 4.** Compositions of samples KAS1 and KAS2 illustrated on a  $K_2O$ - $Al_2O_3$ - $SiO_2$  phase diagram[24].

Reproduced with permission of Calphad, license # 4860380335995.

## 2. Experimental Procedures

### 2.1 Sample Preparation and Compositional Analysis

To explore the effects of  $ZrO_2$  on the crystallization behaviour of glasses that build upon our previous work [16] and which present relevance to glasses developed for their useful properties in the  $K_2O$ - $Al_2O_3$ - $SiO_2$  system [12,13,16], four potassium aluminosilicate glasses (two with  $ZrO_2$  and two without  $ZrO_2$ ) were prepared via melt processing, with their nominal compositions based on two points along the tie-line from  $KAlSiO_4$  to  $Al_2O_3$ , and the tie-line from  $KAlSi_2O_6$  to  $Al_2O_3$  in the  $K_2O$ - $Al_2O_3$ - $SiO_2$  phase diagram separately, as shown in Figure 4. The nominal glass chemical compositions are presented in Table 1. All inorganic raw materials (Table 2) were

weighed according to stoichiometry, then carefully mixed in a mixer prior to melting. Production of glass samples was carried out using a melt-blowing process as described below. A 20 kg batch of each glass composition listed in Table 1 was prepared using a rotary mixer. The batch melting process was conducted using a submerged electrode arc furnace equipped with molybdenum electrodes which drives a high electrical current through the molten glass batch. Initial melting was carried out using an oxy-acetylene torch in order to produce a small, electrically conductive melt between the molybdenum electrodes. The glass melt was contained in a water-cooled stainless-steel furnace (melting temperature 2000-2200 °C, for ~ 2 hours). The furnace was equipped with an orifice at the bottom, allowing a stream of glass melt to be presented to a compressed air nozzle. The compressed air results in atomisation of the molten glass into small droplets and rapid quenching to produce glass particles. The blown material is then directed to a collection chamber through a steel duct. The collection chamber contains a fine mesh made of stainless steel to collect the glass material.

Table 1. Nominal glass compositions in the K<sub>2</sub>O-Al<sub>2</sub>O<sub>3</sub>-SiO<sub>2</sub> mixed with/without

ZrO<sub>2</sub> (wt.%).

	KAS1	KAS1-Z	KAS2	KAS2-Z
Al <sub>2</sub> O <sub>3</sub>	38.8	36.1	45.8	41.6
K <sub>2</sub> O	28.0	26.0	15.1	13.9
SiO <sub>2</sub>	33.2	30.9	39.1	37.3
ZrO <sub>2</sub>	0.0	7.0	0.0	7.2

Table 2. Raw materials used for glass production.

Raw material	Purity	Supplier
Al <sub>2</sub> O <sub>3</sub>	>99.0%	Richard Baker Harrison Ltd.
K <sub>2</sub> CO <sub>3</sub>	>99.5%	Norkem Ltd.
SiO <sub>2</sub>	>99.6%	Sibelco UK Ltd.
ZrSiO <sub>4</sub>	>99.0%	Richards Bay Minerals Ltd.

Heat treatment of the as-produced glass samples was conducted in air using an electric furnace. During the heat treatment experiments, the samples were placed into the furnace at room temperature and the furnace was heated to the selected temperature (1250°C) at a rate of 5°C per minute. Samples were held at temperature for the relevant time period, then removed from the furnace at the same temperature at set time intervals with an accuracy of  $\pm 2$  seconds for 1 and 5 minutes samples;  $\pm 5$  seconds for 15 minutes, 30 minutes and 1 hour samples;  $\pm 5$  minutes for the 24 hours sample. The range of heat treatment times (5 mins, 10 mins, 30 mins, 60 mins and 24 hours) was selected to examine the early formation and evolution of each crystalline phase. The rationale for these relatively short-term experiments (by comparison with our earlier research [16]) was to study the time needed for each composition to transform from amorphous to crystalline, and to consider initial phase developments. To identify the crystalline phases corresponding to exothermic peaks identified from DSC results, heat treatments were also applied to the as-produced glass samples. For these heat treatments, an electric furnace was pre-heated to the selected temperature. Samples were then placed into the furnace and held at this temperature for 2 hours,

then removed from the furnace and air-cooled to room temperature, ready for further XRD characterization.

## 2.2 Characterization and Analysis

Quantitative XRF analysis was carried out using a PANalytical—Axios Advanced X-ray fluorescence spectrometer. Samples were prepared in the form of fused beads: 1.000 ± 0.002 g of sample was carefully weighed and mixed with 10.000 ± 0.002 g di-lithium tetraborate and melted to form a transparent glass disk using an automatic bead making instrument.

Crystallographic evolution arising from the variable heat treatment experiments was investigated by XRD at room temperature, with a diffractometer (model: Empyrean XRD, PANalytical™, Almelo, The Netherlands) equipped with a Cu tube operated at 40 kV and 40 mA, in the  $2\theta$  range between 5 and 90°, with  $2\theta$  increments of 0.016° per step. All samples were analyzed using a reflection spinner sample holder, spinning at 0.25 Hz. All samples were crushed to fine powders using a mortar and pestle prior to measurement.

The thermal behaviour of the samples was investigated by nonisothermal differential scanning calorimetry (DSC). The measurements were performed with a Netzsch STA 449 F5 Jupiter instrument between room temperature and 1400°C, with heating rates between 5 and 40°C/min. All DSC measurements were carried out on 50.0 mg samples against the same mass of 99.9% purity  $\alpha$ -Al<sub>2</sub>O<sub>3</sub>, as an inert reference material, which was calcined at 1450°C for 15 hours prior to measurements.

To determine the activation energy for crystallization from the exothermic peak temperatures obtained from the DSC curves, the Kissinger equation [31] was applied:

$$\ln \frac{a}{T_0^2} = -\frac{E_a}{RT_0} + C \quad (1)$$

where  $a$  is the heating rate,  $E_a$  is the activation energy,  $R$  is the gas constant,  $T_0$  is the exothermic peak temperature in Kelvin, and  $C$  is a constant. The activation energy is calculated from the slope of the line of  $\ln (a/T_0^2)$  vs.  $1/T_0$ .

The crystallization kinetic factor,  $k$ , was also calculated using a modified Johnson-Mehl-Avrami equation (2) [32].

$$k = \gamma \cdot \exp (-E_a/RT) \quad (2)$$

where  $\gamma$  is a frequency factor that can be deduced from (3):

$$\ln \frac{a}{T_0^2} = -\frac{E_a}{RT_0} - \ln \frac{E_a}{R} + \ln \gamma \quad (3)$$

The shape factor ( $n$ ) of the exothermic peak is calculated using (4) [16]:

$$n = \frac{2.5}{\Delta T} \cdot \frac{T_0^2}{\left(\frac{E_a}{R}\right)} \quad (4)$$

where  $n$  is the Avrami constant and  $\Delta T$  is the full width at half maximum (FWHM) of the exothermic peak. Peakfit® software was applied to distinguish overlapped exothermic peak signals and their FWHM. The value of the Avrami constant,  $n$ , provides information regarding the morphology of the growing crystals [16]. The value of  $n$  reveals the dominant mechanism of crystallization. Smaller values of  $n$  indicate that crystallization is controlled by a surface crystallization mechanism instead of volume crystallization, and that the dimension of crystallization is low. The Avrami parameter can be considered to comprise two terms: one that represents the dimension of crystal growth, having integer values of 1, 2 or 3 corresponding to one-,

two- or three-dimensional entities that are formed. The second term relates to the time dependence of nucleation with values of either 0 or 1, where 0 corresponds to instantaneous nucleation and 1 to sporadic nucleation [16]. Additionally, larger values of  $n$  are expected when increase nucleation rates occur, such as in diffusion-controlled reactions ( $>2.5$ ) or in the case of polymorphic transformations ( $>4$ ) [16].

### 3. Results

Elemental analyses (XRF) confirmed (Table 3) that samples KAS1 and KAS2, which have nominal compositions on the eutectic line  $\text{KAlSiO}_4\text{-Al}_2\text{O}_3$  (near to  $\text{KAlSiO}_4$ ) and the eutectic line  $\text{KAlSi}_2\text{O}_6\text{-Al}_2\text{O}_3$  (close to  $\text{KAlSi}_2\text{O}_6$ ), respectively, were closely similar to the analysed compositions. Low but measurable potassium loss, less than 0.7 wt%  $\text{K}_2\text{O}$ , was observed after melting for all 4 glass samples, and can be attributed to volatilization losses during melting [33]. These results confirm that each as-melted glass composition was closely similar to its nominal composition.

Table 3. XRF-analyzed compositions for all glass samples (wt. %)

	KAS1	KAS1-Z	KAS2	KAS2-Z
$\text{Al}_2\text{O}_3$	37.4	35.1	45.7	41.8
$\text{K}_2\text{O}$	27.9	25.7	14.5	13.8
$\text{SiO}_2$	34.7	31.7	39.8	37.3
$\text{ZrO}_2$	0.0	7.5	0.0	7.1

\*Uncertainties associated with the XRF analyses are estimated at  $\pm 2\%$  of measured concentrations.

### 3.1 Thermal Analysis and Phase Identification

To determine the crystallization behaviour of the glasses and explore the activation energies for their crystallization, nonisothermal differential thermal analysis was used. In Figure 5, DSC curves for all samples at different heating rates, from 5°C/min to 40°C/min, are presented. For sample KAS1, only one strong exothermic peak is observed at ~1100°C, which is related to the crystallization of kalsilite. With the introduction of ZrO<sub>2</sub> (sample KAS1-Z), a second exothermic peak appears at ~1000°C, with the exothermic peak at ~1100°C also moving to higher temperatures. For sample KAS2 a weaker exothermic peak occurs at ~1020°C and another peak is observed at ~1350°C. With introduction of ZrO<sub>2</sub> (sample KAS2-Z), a third exothermic peak occurs at ~980°C, near to the ~1020°C exothermic peak, which moves towards high temperatures.

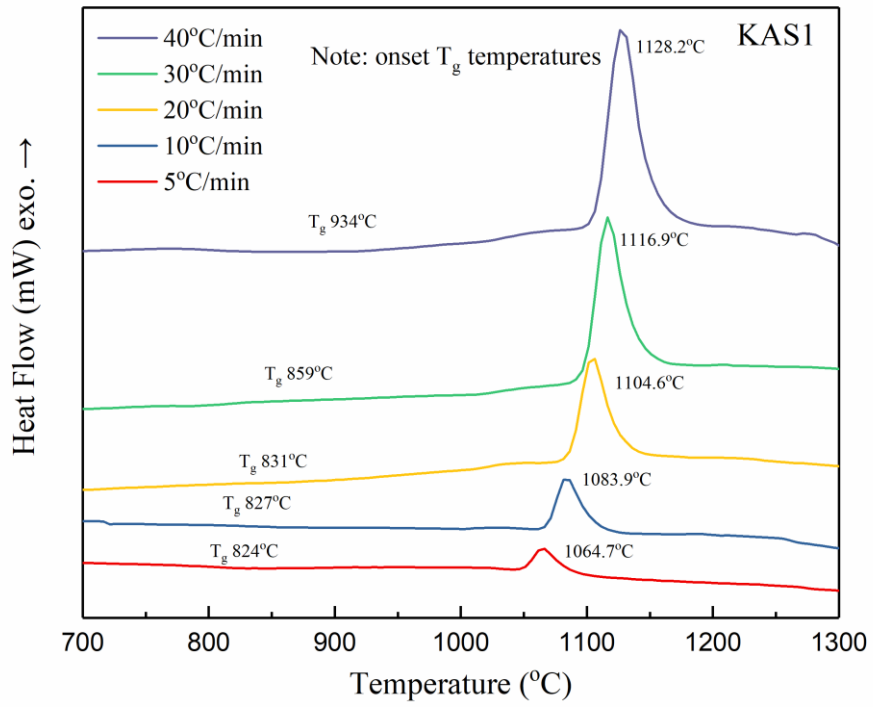


Figure 5. a. DSC curves for KAS1 glass in different heating rates (from 5°C/min to 40°C/min).

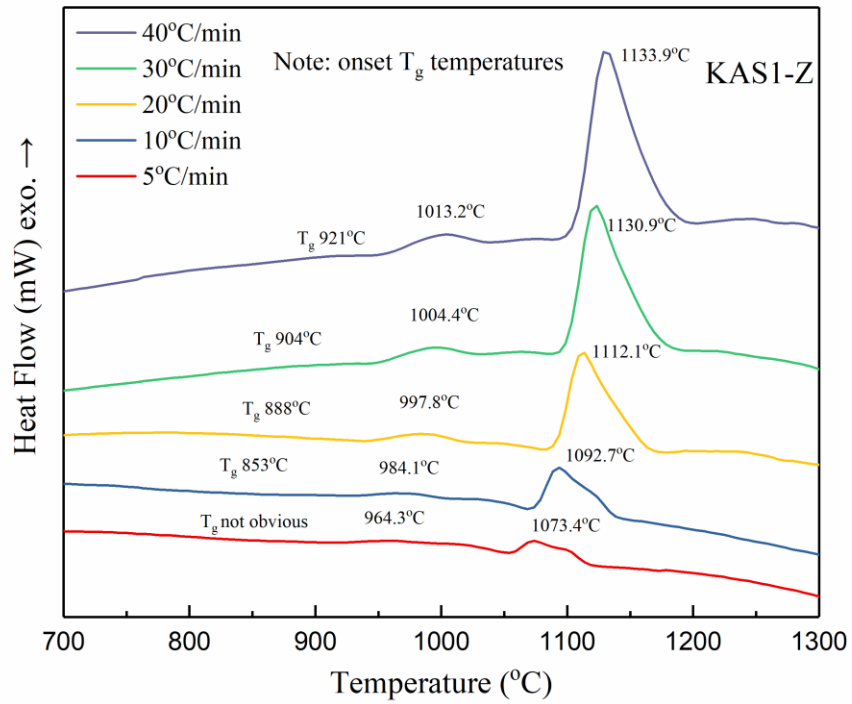


Figure 5. b. DSC curves for KAS1-Z glass in different heating rates (from 5°C/min to 40°C/min).

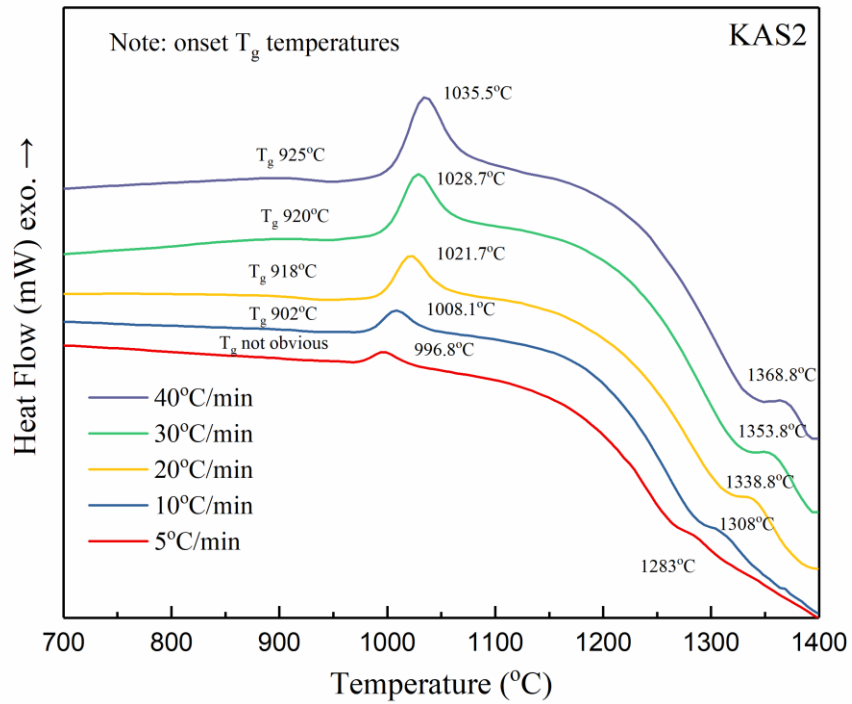


Figure 5. c. DSC curves for KAS2 glass in different heating rates (from 5°C/min to 40°C/min).

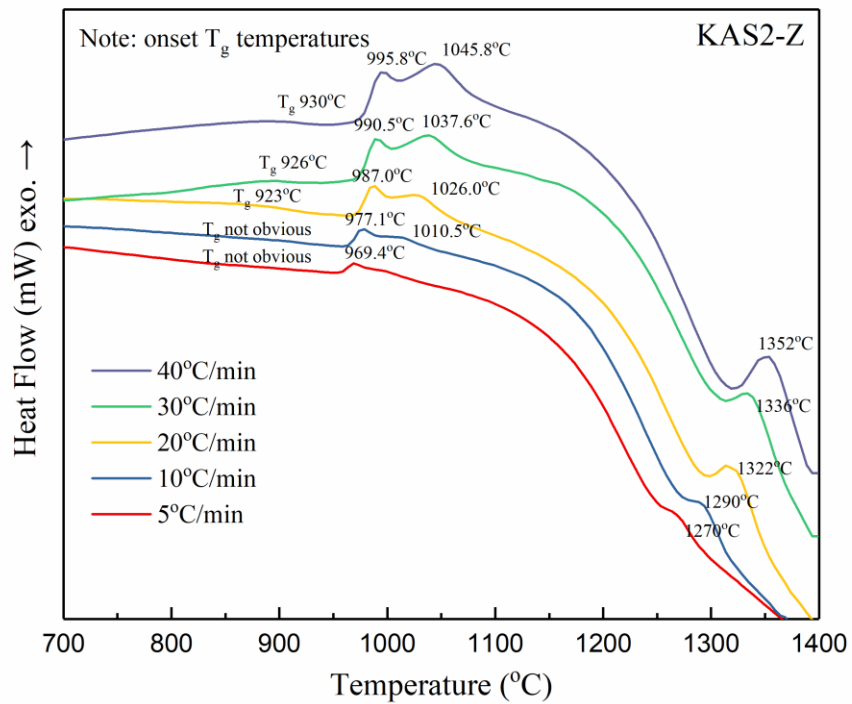
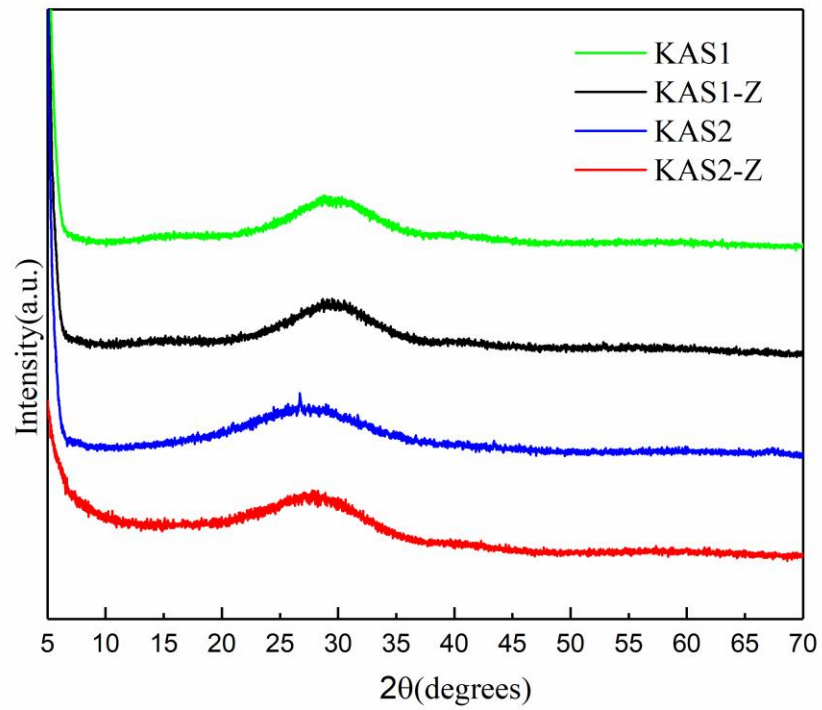


Figure 5. d. DSC curves for KAS2-Z glass in different heating rates (from 5°C/min to 40°C/min).

XRD patterns for as-prepared glass samples are presented in Figure 6. The amorphous nature of the as-prepared samples KAS1, KAS1-Z and KAS2-Z is confirmed. For sample KAS2, a very weak SiO<sub>2</sub> (ICDD 03-065-0466) phase was determined in the as-prepared glass, this was confirmed by XRD observation to be due to imperfect melting of the sand in the raw materials and not to formation post-melting or during cooling. Due to the nature and constraints of the melting technology used here for glass preparation, very small amounts of undissolved silica sand can occasionally arise and are unavoidable. Phases were assigned to the exothermic peak temperatures obtained from DSC analysis through XRD results, which are presented in Figure 7 and Figure 8. According to the XRD patterns for KAS1 and KAS1-Z glasses heat treated at 1250°C (Figure 8 a and b), the exothermic peak observed at ~1100°C can be assigned to the crystallization of kalsilite (K<sub>2</sub>O·Al<sub>2</sub>O<sub>3</sub>·2SiO<sub>2</sub> or KAlSiO<sub>4</sub>) as only one phase is present in the heat-treated KAS1 sample. For sample KAS1-Z, the additional DSC peak at ~1000°C can be attributed to the crystallization of zirconia (ZrO<sub>2</sub>).

For sample KAS2, except SiO<sub>2</sub> phase, a gamma aluminium oxide, γ-Al<sub>2</sub>O<sub>3</sub> (ICDD 00-010-0425), was also identified after 10 minutes' heat treatment at 1020°C (Figure 7a) as the exothermic peak observed at ~1020°C can be assigned to the crystallization of γ-Al<sub>2</sub>O<sub>3</sub>. At 1330°C, leucite (KAlSi<sub>2</sub>O<sub>6</sub> (ICDD 01-071-1147)) was identified as the major phase from the XRD patterns shown in Figure 7b. The second DSC peak for sample KAS2 at 1330°C can be attributed to the crystallization of leucite. Meanwhile for sample KAS2-Z, one additional exothermic peak appeared below 1000°C, which

can be attributed to the crystallization of zirconia ( $ZrO_2$ ).



**Figure 6.** XRD patterns for as prepared glass samples of KAS1, KAS2, KAS1-Z and KAS2-Z.

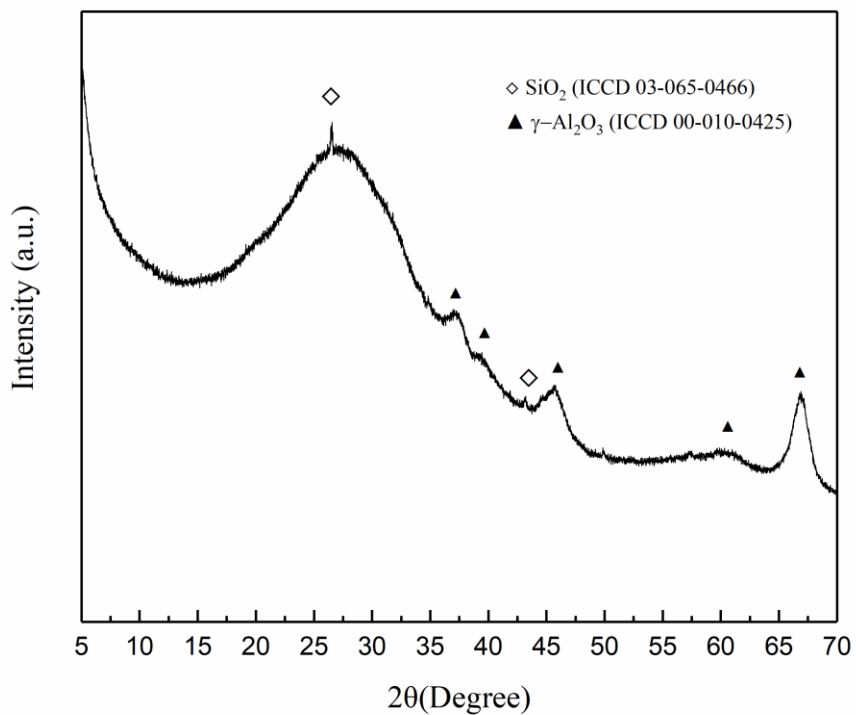


**Figure 7. a.** XRD pattern for sample KAS2 heat treated at 1020°C for 10 mins.

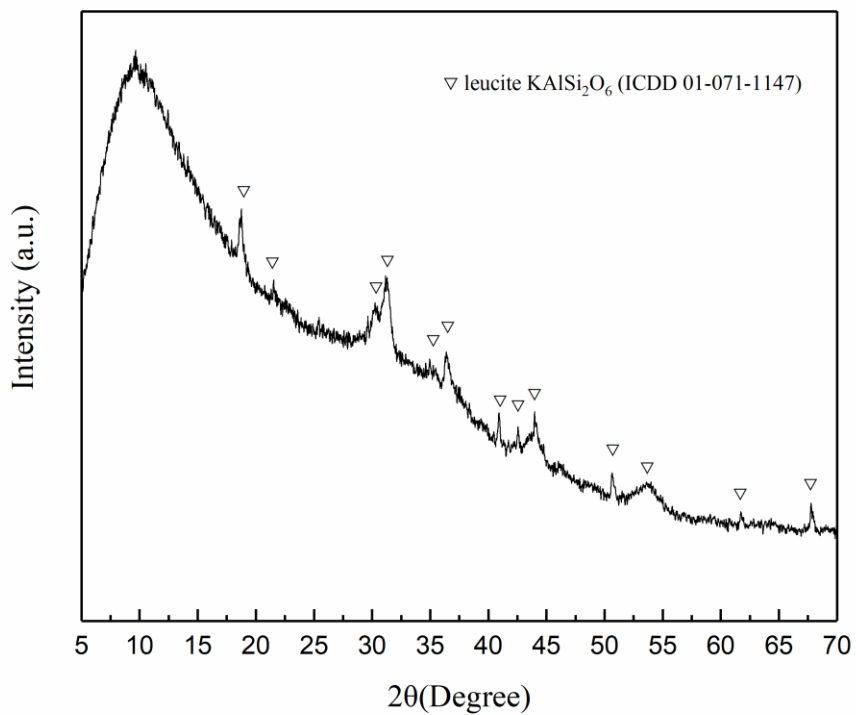


**Figure 7. b.** XRD pattern for sample KAS2 heat treated at 1330°C for 10 mins.

As shown in Table 4, the calculated activation energies ( $E_a$ ) of crystallization vary considerably between the different samples. For sample KAS1,  $E_a$  for the crystallization of kalsilite ( $\text{KAlSiO}_4$ ) is 492.0 kJ/mol. For sample KAS1-Z, the introduction of zirconia ( $\text{ZrO}_2$ ) results in the same  $E_a$  value, within uncertainties, of 494.0 kJ/mol. Meanwhile,  $E_a$  for the crystallization of gamma aluminium oxide ( $\gamma\text{-Al}_2\text{O}_3$ ) decreased from 722.8 kJ/mol for sample KAS2 to 529.7 kJ/mol for sample KAS2-Z. However,  $E_a$  for the crystallization of leucite ( $\text{KAlSi}_2\text{O}_6$ ) shows little change with the introduction of zirconia ( $\text{ZrO}_2$ ), increasing very slightly from 488.6 kJ/mol for sample KAS2 to 496.0 kJ/mol for sample KAS2-Z. When comparing the behaviour of the different glass compositions,  $E_a$  for  $\text{ZrO}_2$  in sample KAS1-Z (559.9 kJ/mol) is substantially lower than for sample KAS2-Z (1018.9 kJ/mol).

Table 4. a. Crystallization activation energy for different glass samples.

Glass	$E_a$ for Peak 1 <sup>†</sup> (kJ/mol)	$E_a$ for Peak 2 <sup>†</sup> (kJ/mol)	$E_a$ for Peak 3 <sup>†</sup> (kJ/mol)
KAS1	-	492.0 / $\text{KAlSiO}_4$	-
KAS1-Z	559.9 / $\text{ZrO}_2$	494.0 / $\text{KAlSiO}_4$	-
KAS2	-	722.8 / $\gamma\text{-Al}_2\text{O}_3$	488.6 / $\text{KAlSi}_2\text{O}_6$
KAS2-Z	1018.9 / $\text{ZrO}_2$	529.7 / $\gamma\text{-Al}_2\text{O}_3$	496.0 / $\text{KAlSi}_2\text{O}_6$

<sup>†</sup> Peak number is according to the order of appearance, with increasing temperature, of exothermic peaks from DSC.

Table 4. b. Average shape factor ( $n$ ) for different crystallisation events.

Glass	Shape factor for Peak 1 <sup>†</sup> ( $n \pm 0.1$ )	Shape factor for Peak 2 <sup>†</sup> ( $n \pm 0.1$ )	Shape factor for Peak 3 <sup>†</sup> ( $n \pm 0.1$ )
KAS1	\	3.6 / $\text{KAlSiO}_4$	\

KAS1-Z	1.4/ ZrO <sub>2</sub>	2.3/ KAlSiO <sub>4</sub>	\
KAS2	\	1.6/ $\gamma$ -Al <sub>2</sub> O <sub>3</sub>	4.2/ KAlSi <sub>2</sub> O <sub>6</sub>
KAS2-Z	2.1/ ZrO <sub>2</sub>	1.3/ $\gamma$ -Al <sub>2</sub> O <sub>3</sub>	3.5/ KAlSi <sub>2</sub> O <sub>6</sub>

† Peak number is defined according to order of occurrence, with increasing temperature, of exothermic peaks from DSC.

### 3.2 Heat Treatment and X-ray Powder Diffraction

XRD patterns for all glass samples after heat treatment at 1250°C for different times are shown in Figure 8. For samples KAS1 and KAS1-Z, kalsilite (KAlSiO<sub>4</sub>) is present at all heat treatment times as the major phase with high crystallinity and similar diffraction peak relative intensities. In addition, zirconia (ZrO<sub>2</sub>) crystallized in sample KAS1-Z after only 5 minutes' heat treatment. The main diffraction peak (101) of ZrO<sub>2</sub> at 30.3° 2 $\theta$  can be observed in all sample KAS1-Z diffraction patterns. With increasing heat treatment time, the (101) peak intensity slightly increased and the full width half-maximum (FWHM) decreased, indicating the degree of crystallinity of zirconia (ZrO<sub>2</sub>) increased with increasing heat treatment time.

For sample KAS2, a sharp diffraction peak (101) attributed to silicon dioxide ( $\alpha$ -SiO<sub>2</sub>) at 26.7° 2 $\theta$  and six weak peaks attributed to gamma aluminium oxide ( $\gamma$ -Al<sub>2</sub>O<sub>3</sub>) were observed at 5 minutes' heat treatment (the SiO<sub>2</sub> peaks, as discussed earlier, confirmed as being due to from relict undissolved SiO<sub>2</sub> from the raw materials). With increasing heat treatment time, peaks for alpha aluminium oxide ( $\alpha$ -Al<sub>2</sub>O<sub>3</sub>) appears after 10 minutes as the  $\gamma$ -Al<sub>2</sub>O<sub>3</sub> polymorph undergoes its transformation, possibly via the  $\theta$ -Al<sub>2</sub>O<sub>3</sub> polymorph [34]. Leucite (KAlSi<sub>2</sub>O<sub>6</sub>) is present after 30 minutes' heat treatment as the major phase. Meanwhile, the diffraction peaks attributed to silicon

dioxide ( $\text{SiO}_2$ ), as illustrated by the non-overlapping peak at  $50.1^\circ 2\theta$ , are absent beyond 30 minutes, indicating that this relict  $\text{SiO}_2$  undergoes reaction with other components to form resulting phases, most likely leucite. After 30 minutes' heat treatment, the peak intensity for leucite ( $\text{KAlSi}_2\text{O}_6$ ) increased with increasing time and the humped background indicative of the presence of an amorphous phase decreased, suggesting ongoing crystallisation of leucite from the glass.

With addition of zirconia (sample KAS2-Z), a measurable amount of  $\text{ZrO}_2$  had crystallised after 5 minutes' heat treatment along with a low level of  $\gamma\text{-Al}_2\text{O}_3$ . Another alpha aluminium oxide ( $\alpha\text{-Al}_2\text{O}_3$ ) phase appears after 30 minutes and there was no indication of the silicon dioxide ( $\alpha\text{-SiO}_2$ ) phase, confirming this sample was free from relict  $\text{SiO}_2$ . For sample KAS2-Z, high intensity diffraction peaks for leucite ( $\text{KAlSi}_2\text{O}_6$ ) were present after 30 minutes' heat treatment and a reduced amorphous hump was observed compared to the diffraction pattern for sample KAS-2. The leucite peak intensity appears to, consistently, increase with further heat treatment time. As was the case for sample KAS1-Z, low levels of both  $\gamma\text{-Al}_2\text{O}_3$  (or the intermediate  $\theta\text{-Al}_2\text{O}_3$ ) and  $\alpha\text{-Al}_2\text{O}_3$  were present after 24 hours at  $1250^\circ\text{C}$ .

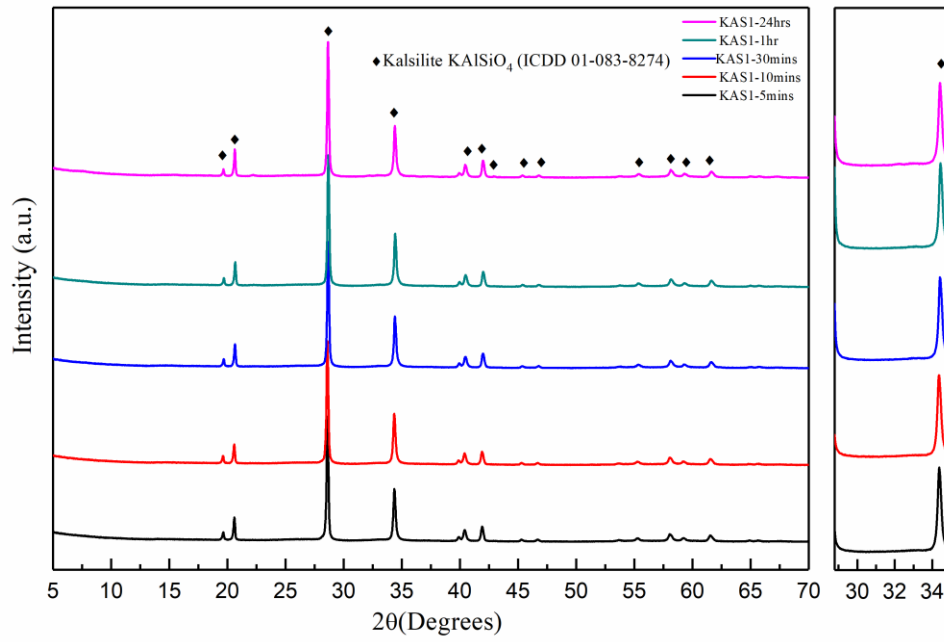


**Figure 8. a.** XRD patterns for samples KASI heat treated at 1250°C from 5 minutes to 24 hours.

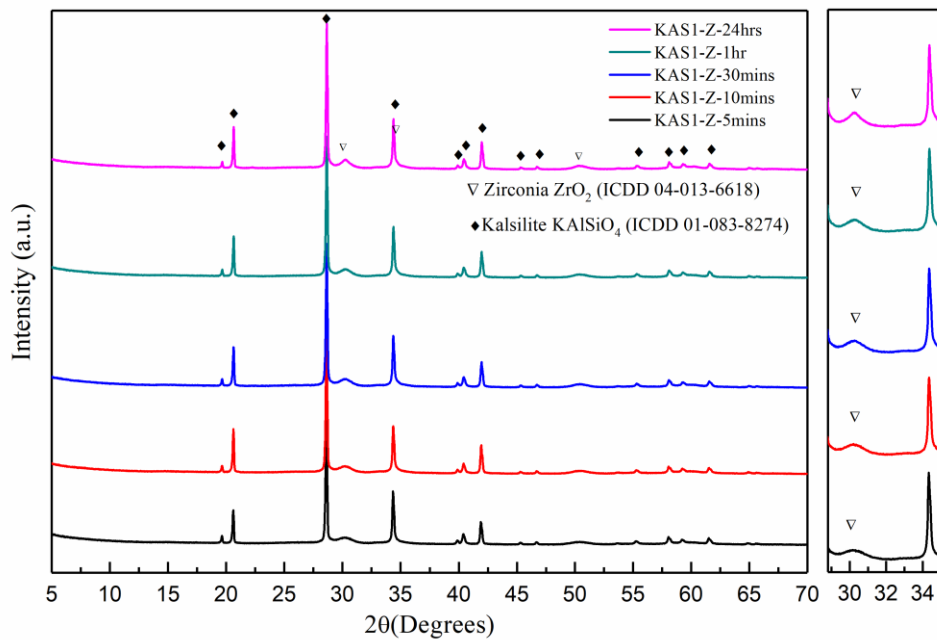


**Figure 8. b.** XRD patterns for samples KASI-Z heat treated at 1250°C from 5 minutes to 24 hours.

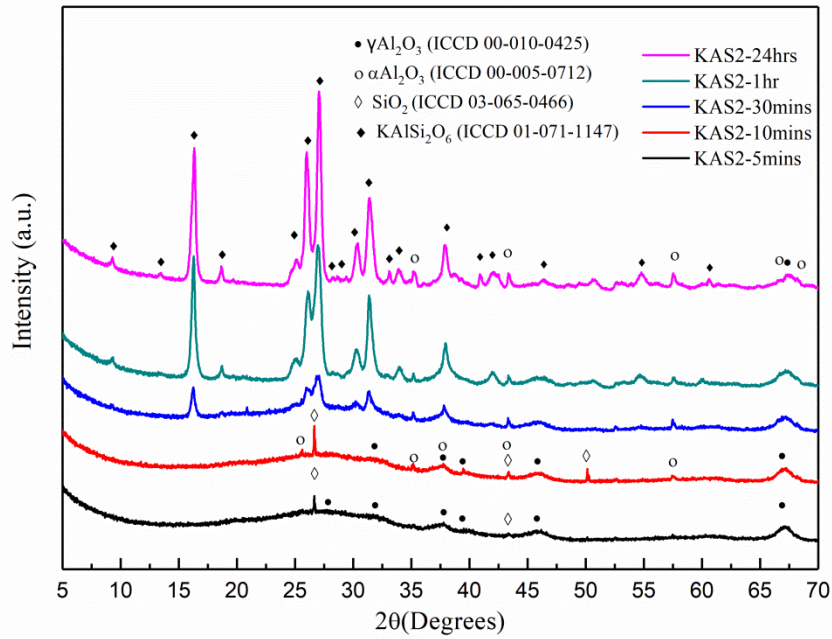


Figure 8. c. XRD patterns for samples KAS2 heat treated at 1250°C from 5 minutes to 24 hours.

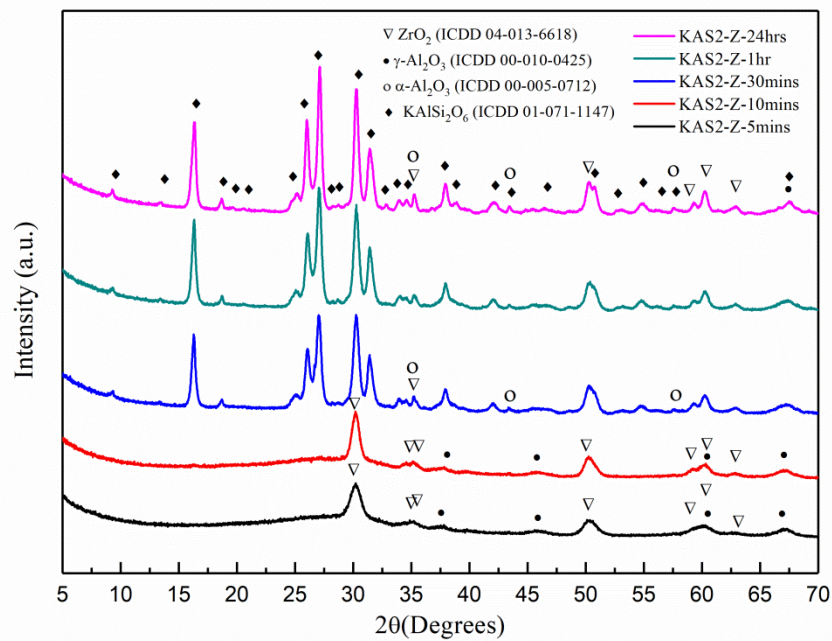


Figure 8. d. XRD patterns for samples KAS2-Z heat treated at 1250°C from 5 minutes to 24 hours.

#### 4. Discussion

## 4.1 Phase Relations

From previous research and phase diagram studies, some information on glass stability in the  $K_2O-Al_2O_3-SiO_2$  system is available. For instance, the phase diagram of the  $KAlSiO_4$  (kalsilite) -  $Al_2O_3$  and  $KAlSi_2O_6$  (leucite) -  $Al_2O_3$  systems from Schairer and Bowen [14] indicates the liquidus phase line with single-phase liquid above it. More recently Yazhenskikh *et al.* [24] and Kim *et al.* [35] presented evaluation and thermodynamic studies of the  $K_2O-Al_2O_3-SiO_2$  system. In their studies, particular phases “liquid+high temperature phase  $KAlSiO_4$ ” and “slag” were labelled above the liquidus phase line in the “binary” phase diagrams of the  $KAlSiO_4 - Al_2O_3$  and  $KAlSi_2O_6 - Al_2O_3$  systems, which indicates a propensity for melt instability and / or rapid devitrification during melt quenching.

In terms of the samples studied here, samples KAS1 and KAS2 sit on the tie-line from  $KAlSiO_4$  to  $Al_2O_3$  and  $KAlSi_2O_6$  to  $Al_2O_3$ , respectively, in the  $K_2O-Al_2O_3-SiO_2$  ternary phase diagram, with compositions close to each of the “binary” phases of the  $KAlSiO_4 - Al_2O_3$  and  $KAlSi_2O_6 - Al_2O_3$  systems noted above. Thus, these two glasses can reasonably be expected to show rapid tendency for devitrification during quenching. For the other as-prepared glasses, the XRD results show no sign of crystallinity with only characteristic amorphous humps in the diffraction patterns (with the exception of the relict  $SiO_2$  discussed previously), confirming these samples were essentially X-ray amorphous. However, when sample KAS1 was heat treated at  $1250^\circ C$  for just 5 minutes (Figure 8a), almost complete crystallization to form kalsilite ( $KAlSiO_4$ ) occurred, as shown in the diffraction pattern; and its absolute

diffraction peak intensity (at  $28.6^\circ 2\theta$ , under the same measurement conditions) increased only very slightly from this after 24 hours' heat treatment. The crystallization of kalsilite ( $\text{KAlSiO}_4$ ) in sample KAS1 is in accordance with the prediction from the phase diagram [24,35]. With the introduction of  $\text{ZrO}_2$ , the crystallization behaviour of kalsilite ( $\text{KAlSiO}_4$ ) in sample KAS1-Z (Figure 8b) is almost the same as in sample KAS1, except that for the strongest diffraction peak of kalsilite at  $28.6^\circ 2\theta$  for sample KAS1-Z, unlike sample KAS1, has an absolute intensity after 5 minutes' heat treatment already roughly the same as the intensity after 24 hours' heat treatment at  $1250^\circ\text{C}$ , again indicating even more rapid crystallisation of kalsilite in sample KAS1-Z than in sample KAS-1.

For sample KAS2, during the heat treatment at  $1250^\circ\text{C}$ , relict  $\text{SiO}_2$  from imperfect raw materials reaction during melting, was present at up to 10 minutes' heat treatment at  $1250^\circ\text{C}$ . The crystallization of gamma aluminium oxide ( $\gamma\text{-Al}_2\text{O}_3$ ) occurred rapidly after 5 minutes' heat treatment, and a further transformation from  $\gamma\text{-Al}_2\text{O}_3$  to  $\alpha\text{-Al}_2\text{O}_3$  (via the intermediate  $\theta\text{-Al}_2\text{O}_3$  polymorph) [36] occurred by 10 minutes' heat treatment, as shown in Figure 8c. Between 30 minutes' to 24 hours' heat treatment at  $1250^\circ\text{C}$  in samples KAS2 the primary phase, leucite ( $\text{KAlSi}_2\text{O}_6$ ), crystallises and continuously grows with coexisting  $\gamma\text{-Al}_2\text{O}_3$  and  $\alpha\text{-Al}_2\text{O}_3$ . However, the diffraction peaks for  $\text{SiO}_2$ , as illustrated by the peak at  $50.2^\circ 2\theta$ , were no longer present after 30 minutes' heat treatment, with the emergence of leucite ( $\text{KAlSi}_2\text{O}_6$ ) indicating that the  $\text{SiO}_2$  participates in, and is consumed by, the formation of leucite ( $\text{KAlSi}_2\text{O}_6$ ). A possible reaction path of  $\text{SiO}_2 + \text{Al}_2\text{O}_3 \rightarrow \text{Al}_6\text{Si}_2\text{O}_{13}$  (mullite) was also considered here

and cannot be definitively ruled out due to the low diffraction peak intensities and the multiple overlapping lines. However, no definitive evidence for the presence of mullite can be found in any diffraction pattern for this sample, even following 24 hours' heat treatment.

Although the minor phase transformation from  $\gamma$ -Al<sub>2</sub>O<sub>3</sub> to  $\alpha$ -Al<sub>2</sub>O<sub>3</sub> in sample KAS2 was identified by XRD following heat treatment at 1250°C, no thermal peaks / signals in DSC traces can be attributed to it, as only two crystallization exothermic peaks were identified, and have been attributed to the crystallization of  $\gamma$ -Al<sub>2</sub>O<sub>3</sub> and leucite as discussed above.

With the introduction of ZrO<sub>2</sub> to the glass a significant amount of crystalline ZrO<sub>2</sub> phase is present after only 5 minutes' heat treatment at 1250°C with gamma aluminium oxide,  $\gamma$ -Al<sub>2</sub>O<sub>3</sub>, present as a minor phase. After 30 minutes' heat treatment, leucite (KAlSi<sub>2</sub>O<sub>6</sub>) was present as the major crystalline phase with ZrO<sub>2</sub>, the presence of  $\alpha$ -Al<sub>2</sub>O<sub>3</sub> was delayed from 10 minutes' in KAS2 to 30 minutes' heat treatment, which indicates that the transformation from  $\gamma$ -Al<sub>2</sub>O<sub>3</sub> to  $\alpha$ -Al<sub>2</sub>O<sub>3</sub> may have been suppressed by the introduction of ZrO<sub>2</sub>. If we compare diffraction patterns after 30 minutes' heat treatment for samples KAS2 and KAS2-Z, the absolute diffraction intensities of the leucite (KAlSi<sub>2</sub>O<sub>6</sub>) peaks for sample KAS2-Z are greater than for sample KAS2, which indicates that the introduction of ZrO<sub>2</sub> promotes crystallization of, and increases the crystallization rate of, leucite (KAlSi<sub>2</sub>O<sub>6</sub>). The intensity of the amorphous hump also appears to be reduced more quickly during heat treatment at 1250°C in sample KAS2-Z compared with sample KAS2, further supporting this

conclusion.

Previous research within the  $K_2O-Al_2O_3-SiO_2$  ternary system has principally focussed on the liquidus surface [14,24,35] with less consideration of the subliquidus phases. Kingery *et al.* [1] presented a partial isothermal section in this ternary phase diagram (Figure 3) at  $1200^\circ C$ , which illustrates the crystallization tendency of alumina ( $Al_2O_3$ ), leucite ( $KAlSi_2O_6$ ) and kalsilite ( $KAlSiO_4$ ) in the delta-shaped region of  $KAS_4-KAS_2-Al_2O_3$  that is in accordance with the crystallization phases,  $Al_2O_3$  and leucite, during the heat treatment of sample KAS2 here. However, for sample KAS1, the composition is closer to the  $K_2O$ -rich range, which has received less attention than the compositional region inhabited by sample KAS2. Kim *et al.* [35] presented a “binary”  $KAlSiO_4-Al_2O_3$  phase diagram (with compositional range including compositions similar to that of sample KAS2) in their work that indicates a phase field of  $KAlSiO_4$  (kalsilite) +  $Al_2O_3$  and  $\beta-Al_2O_3$  in the temperature range  $500^\circ C$  to  $1700^\circ C$ . In this study, for sample KAS2, kalsilite ( $KAlSiO_4$ ) and aluminium oxides (in the form of  $\gamma-Al_2O_3$  and  $\alpha-Al_2O_3$ ) were characterized during heat treatment.

## 4.2 Thermal Analysis

To fully explore and determine the crystallization temperature and thermal stability of glasses, DSC at multiple heating rates was applied here. Attributions of thermal peaks to the crystallization of phases are fully presented above with the calculated activation energy of crystallization,  $E_a$ , given in Table 4a. There is some difficulty in reconciling some of these results with the observed crystallisation behaviour from

XRD. For example, the introduction of  $\text{ZrO}_2$  appears to have little effect on  $E_a$  of leucite ( $\text{KAlSi}_2\text{O}_6$ ), which increased only slightly from 488.0 kJ/mol (sample KAS2) to 496.0 kJ/mol (sample KAS2-Z). However, XRD results strongly suggest that addition of  $\text{ZrO}_2$  increases the crystallization rate of leucite during heat treatment, as shown in Figure 8. Also,  $E_a$  of crystallisation for  $\text{ZrO}_2$  in sample KAS2-Z is approximately double that for sample KAS1-Z, yet similar  $\text{ZrO}_2$  signatures and intensities were observed in the relevant diffraction patterns. Concerning shape factors ( $n$ ) as given in Table 4b, the addition of  $\text{ZrO}_2$  affects and decreases  $n$  of other crystalline phases in the KAS1 and KAS2-Z series. Specifically, the shape factor  $n$  for  $\text{KAlSiO}_4$  decreases from 3.6 to 2.3 from sample KAS1 to sample KAS1-Z, which indicates a shift in the crystallisation mechanism of  $\text{KAlSiO}_4$  from volume nucleation and 2-dimensional (2D) crystal growth in sample KAS1 towards surface nucleation with 1D crystal growth in sample KAS1-Z. Meanwhile,  $n$  decreases from 1.6 to 1.3 for  $\gamma\text{-Al}_2\text{O}_3$  and from 4.2 to 3.5 for  $\text{KAlSi}_2\text{O}_6$  from sample KAS2 to sample KAS2-Z. Accordingly, the crystallisation mechanism of  $\text{KAlSi}_2\text{O}_6$  shifts from volume nucleation and 3D crystal growth towards volume nucleation and 2D crystal growth.

If the crystal growth rate is diffusion-controlled, the activation energy for crystal growth  $E_a$  can be related to that for viscous flow in the similar temperature range [37]. However, as noted previously, the XANES study of Ficheux *et al.* [30] suggests that the introduction of  $\text{ZrO}_2$  can increase the network modifier ionic diffusivity as well as viscosity in melts at high temperature, which offers a potential explanation for the lack of clear correlation between crystallization tendency (glass-forming ability) and

$E_a$  compared to other glass system. Accordingly, the reliability of the Avrami number (shape factor,  $n$ ) calculated based on activation energy,  $E_a$  is thus limited in this case.

On the other hand, thermal analysis has been widely applied in the study of glass crystallization kinetics, and a number of analytical methods have been developed [32]. Whilst there is no clear consensus on which method or criterion is most widely applicable, the most commonly used criterion is crystallization activation energy ( $E_a$ ), which can be determined from DSC/DTA measurements. According to this criterion, a higher  $E_a$  indicates a lower crystallization tendency. However, it has been found that in some cases the  $E_a$  criterion indicates behaviour that is not reflected in experimental results for some high crystallization tendency systems such as fluoride glasses [37,38] and high-TiO<sub>2</sub> glasses [32]. It thus appears that, in this case, the glasses in the K<sub>2</sub>O-Al<sub>2</sub>O<sub>3</sub>-SiO<sub>2</sub> system studied here can also be included. Hu *et al.* [32] put forward a kinetic factor  $k$ , from the activation energy of crystallization, based on a modified Johnson-Mehl-Avrami equation and verified for fluoride glasses and TiO<sub>2</sub>-B<sub>2</sub>O<sub>3</sub>-BaO-CaO glasses. We have applied this factor  $k$  here (Table 6). In addition to activation energy and parameters derived from it, a number of other criteria for thermal stability or glass formation tendency have been interpreted from characteristic temperatures by DTA or DSC in previous research [39–42]. Historically, Dietzel [43] suggested that characteristic temperatures are available for glass stability prediction. It was experimentally observed that the temperature difference ( $\Delta T$ ) between onset crystallization temperature ( $T_x$ ) and glass transition temperature ( $T_g$ ) has a relationship with glass stability. Uhlmann [44] indicated that a high glass viscosity at the

crystalline phase melting point and / or a rapidly rising viscosity with falling temperature below the melting point are beneficial for glass formation. He developed the equation  $T_{rg} = T_g/T_m$  (or  $T_g/T_l$ , where  $T_m$  is melting temperature and  $T_l$  is liquidus temperature) as the one of the earliest criteria to evaluate the stability of glass. In 1989, Weinberg *et al.* [45] developed the term critical cooling rate ( $R_c$ ) for glass stability assessments. In 1972, a glass-forming coefficient,  $K_H$ , was developed by Hrubý [46]. This coefficient is related to  $T_x$ ,  $T_g$  and  $T_m$ . A limitation for  $T_{rg}$  is it may fail to accurately predict glass stability in some cases [47,48]. Nascimento *et al.* [49] indicated that in glasses for which the glass transition temperature shows a weaker correlation with glass-forming ability,  $T_{rg}$  has less correlation with glass stability compare to  $K_H$ . However, good correlation between glass stability and  $K_H$  is generally provided by oxide glasses [50,51]. Further studies include Weinberg's  $K_W$  criterion [52] and Lu and Liu's  $K_{LL}$  criterion [53,54], all based on these three characteristic temperatures ( $T_x$ ,  $T_g$  and  $T_m$ ) and showing good correlation with glass stability. According to Kozmidis-Petrovic *et al.* [39], among all criteria interpreted from characteristic temperatures, Hrubý's  $K_H$  provides excellent correlation with glass stability in oxide glasses and Weinberg's  $K_W$  is ranked close behind. Most recently, Jeanini *et al.* [55] presented detailed statistical comparisons of 23 different published glass stability criteria based on the characteristic temperatures. Through their work on the data for 12 stoichiometric oxide glasses, it was concluded that Weinberg's  $K_W$  criterion ranked first, closely followed by the Hrubý's  $K_H$  and Lu-Liu's  $K_{LL}$ . All of these studies reveal the complexity and difficulty of identifying a universal criterion

for all glasses. Instead of using one criterion, consideration of multiple criteria may thus be useful.

One challenge, for the glasses studied here, is that the liquidus temperatures of large parts of the  $\text{K}_2\text{O}-\text{Al}_2\text{O}_3-\text{SiO}_2$  system are very high: beyond the capability of most DSC equipment and furnaces to measure. Fortunately, the  $\text{K}_2\text{O}-\text{Al}_2\text{O}_3-\text{SiO}_2$  system has been thermodynamically modelled by Yazhenshikh *et al.* [24] so some data is available. The liquidus temperatures of samples KAS1 and KAS2 can be directly estimated from their calculations, and regarded as equivalent to melting temperature: these are listed in Table 5. As discussed earlier, there is general consensus that introducing or increasing the content of  $\text{ZrO}_2$  in silicate glasses tends to increase both the viscosity and liquidus temperature [26,33,56]. Accordingly, it is reasonable to assume that the liquidus temperatures ( $T_m$ ) of samples KAS1-Z and KAS2-Z will be higher than those of the  $\text{ZrO}_2$ -free samples KAS1 and KAS2.

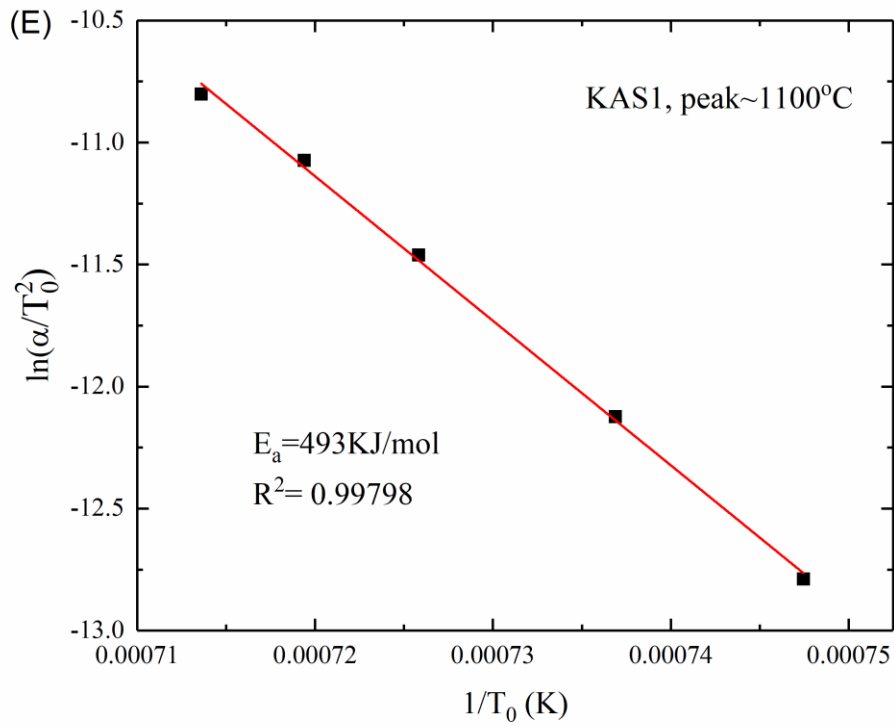


Figure 9. a. Kissinger plots for non-isothermal crystallization of KAlSiO<sub>4</sub> in sample KAS1.

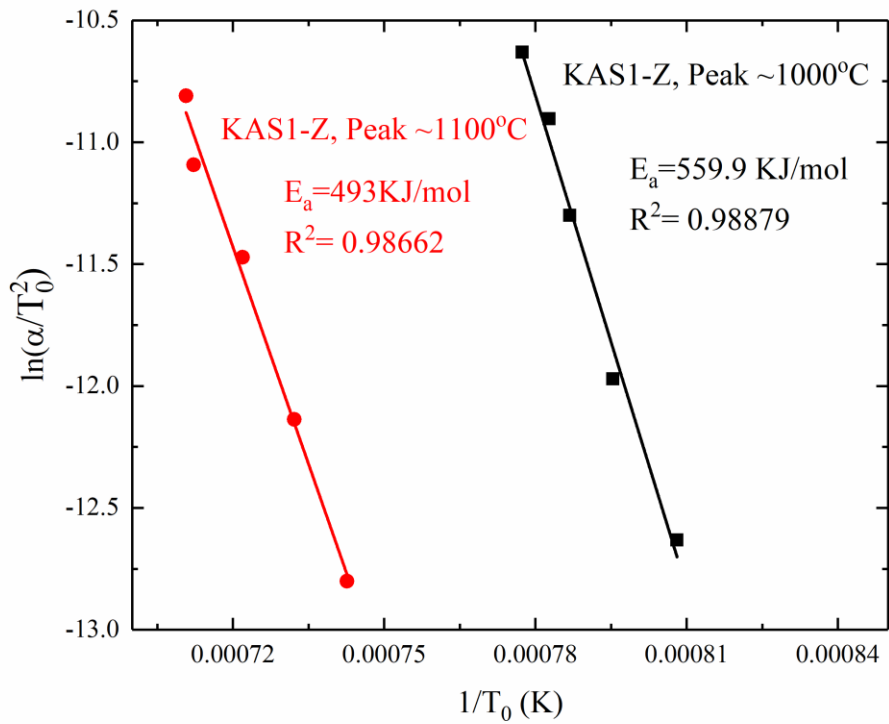


Figure 9. b. Kissinger plots for non-isothermal crystallization of ZrO<sub>2</sub> at ~1000°C and KAlSiO<sub>4</sub> at ~1100°C in

sample KAS1-Z.

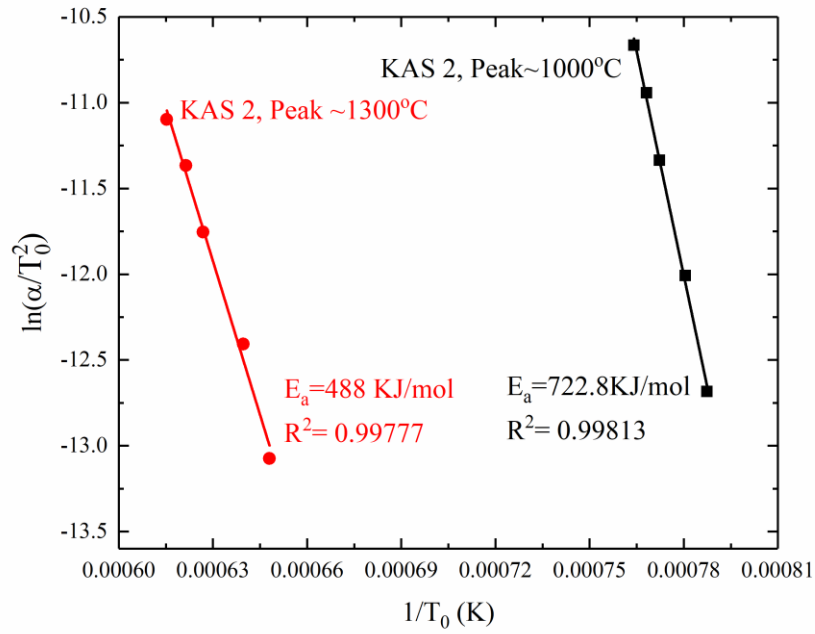


Figure 9. c. Kissinger plots for non-isothermal crystallization of  $\gamma\text{-Al}_2\text{O}_3$  at  $\sim 1000^\circ\text{C}$  and  $\text{KAlSi}_2\text{O}_6$  at  $\sim 1300^\circ\text{C}$  in sample KAS2.

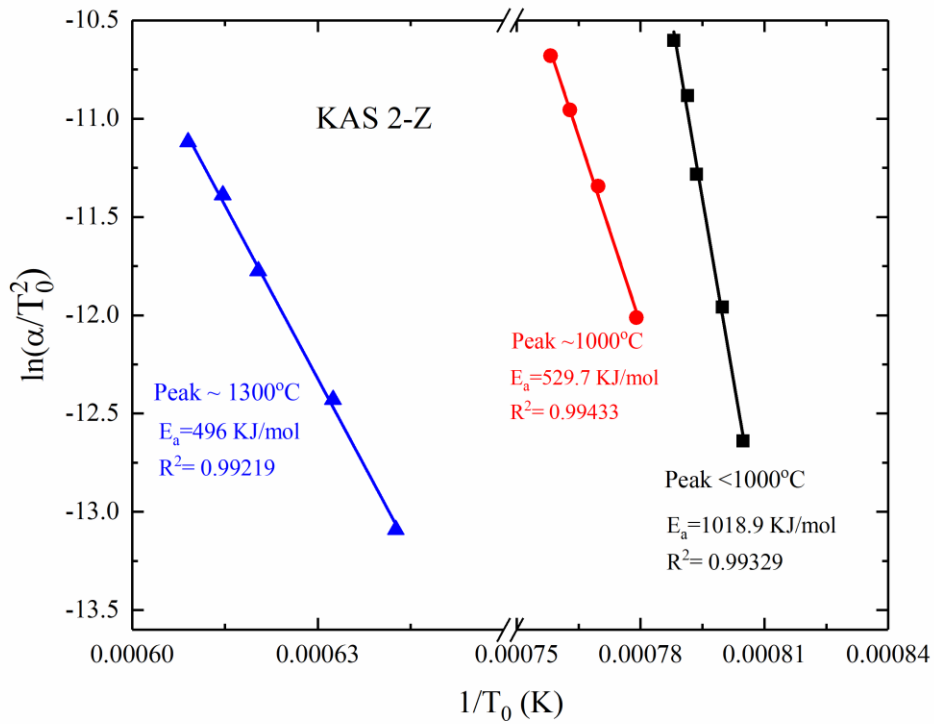


Figure 9. d. Kissinger plots for non-isothermal crystallization of  $\text{ZrO}_2 < 1000^\circ\text{C}$ ,  $\gamma\text{-Al}_2\text{O}_3$  at  $\sim 1000^\circ\text{C}$  and

KAlSi<sub>2</sub>O<sub>6</sub> at ~1300 °C in sample KAS2-Z.

Table 5

Table 6

Glass stability criteria including  $K_H$ ,  $K_W$ ,  $K_{LL}$  and  $k$  were calculated and are listed in Table 6. Those criteria for samples KAS1 and KAS2 can be calculated directly from the characteristic temperatures listed in Table 5. For samples KAS1-Z and KAS2-Z, the unknown  $T_m$  was replaced by those of samples KAS1 and KAS2 for criteria calculation. Accordingly, the uncertainties on these analyses are greater and their real values are expected to be lower than calculated due to the expected higher liquidus temperature ( $T_l$ ) of samples KAS1-Z and KAS2-Z. The introduction of ZrO<sub>2</sub> in sample KAS1-Z reduced  $K_H$  of kalsilite (KAlSiO<sub>4</sub>) from 0.3591 to less than 0.2881, which decreases the glass stability and thus promotes the crystallization of kalsilite (KAlSiO<sub>4</sub>). Meanwhile, the introduction of ZrO<sub>2</sub> in sample KAS2-Z also reduced  $K_H$  of gamma aluminium oxide ( $\gamma$ -Al<sub>2</sub>O<sub>3</sub>) and leucite (KAlSi<sub>2</sub>O<sub>6</sub>) from 0.0992 to less than 0.069 and from 0.8837 to less than 0.7923, respectively. The glass stability of sample KAS2-Z is thus decreased relative to sample KAS2, and crystallization of aluminium oxides and leucite are promoted accordingly. The  $K_H$  values for ZrO<sub>2</sub> in samples KAS1-Z and KAS2-Z are almost equal, which indicates that the crystallization behaviour of ZrO<sub>2</sub> in those two different glasses will be similar. The calculated  $K_W$  and  $K_{LL}$  also show consistency. Thus we can consider and compare those criteria with Hu *et al.*'s [32] kinetic factor  $k$ , which was deduced from the activation energy of crystallization. Although the source for derivation is different, the variation tendency of  $k$  is consistent with  $K_H$ ,  $K_W$  and  $K_{LL}$ , which broadly supports the validity of these

criteria.

## 5. Conclusions

The thermal stability and crystallization behaviours of two glass-forming compositions in the  $K_2O-Al_2O_3-SiO_2$  ternary system were studied without  $ZrO_2$  (samples KAS1 and KAS2) and with  $ZrO_2$  (samples KAS1-Z and KAS2-Z) additions. The amorphous nature of as-prepared glasses was confirmed by XRD except a weak phase  $SiO_2$  in KAS2, attributable to relict  $SiO_2$  from the raw materials. Full crystallization of kalsilite was observed in sample KAS1 after only 5 minutes' heat treatment at  $1250^\circ C$ , and leucite began to form in sample KAS2 after 30 minutes' heat treatment. With the introduction of  $ZrO_2$ , the promotion of kalsilite and leucite crystallization was observed in samples KAS1-Z and KAS2-Z, respectively. Through DSC measurements, there was no clear correlation between crystallization tendency (glass-forming ability) and calculated crystallization activation energy  $E_a$  for these high crystallization tendency glasses. Furthermore, multiple glass stability (GS) parameters (Hrubý  $K_H$ , Weinberg  $K_W$ , Lu & Liu  $K_{LL}$ ) were calculated based on characteristic temperatures and a further criterion (Hu  $k$ ) was calculated based on  $E_a$ . The validity of these criteria was cross validated with one another and the promotion of crystallization in these glasses by addition of  $ZrO_2$  was confirmed through these criteria.

## **Acknowledgements**

The authors acknowledge with thanks useful discussions and input from Gary A. Jubb and Amanda Quadling, and financial support from Morgan Advanced Materials Ltd.

## References

- [1] Kingery, W. D., Bowen, H. K., Uhlmann, D. R. Introduction to ceramics (2<sup>nd</sup> Ed.), John Wiley & Sons, Canada, 1976.
- [2] Heimann, R. B. Classic and Advanced Ceramics: From Fundamentals to Applications, John Wiley & Sons, Betz Druck GmbH, Darmstadt, 2010.
- [3] Höland, W., Rheinberger, V., Apel, E., van't Hoen, C. Principles and phenomena of bioengineering with glass-ceramics for dental restoration. *J. Eur. Ceram. Soc.*, 2007, **27**(2–3), 1521–1526.
- [4] Schneider, H., Schreuer, J., Hildmann, B. Structure and properties of mullite—a review. *J. Eur. Ceram. Soc.*, 2008, **28**(2), 329–344.
- [5] Aksay, I. A., Dabbs, D.M., Sarikaya, M. Mullite for Structural, Electronic, and Optical Applications. *J. Am. Ceram. Soc.*, 1991, **74**(10), 2343–2358.
- [6] Boch, P., Chartier, T. Tape casting and properties of mullite and zirconia–mullite ceramics. *J. Am. Ceram. Soc.*, 1991, **74**(10), 2448–2452.
- [7] Prochazaka, S., Wallace, J. S. Claussen, N. Microstructure of sintered mullite-zirconia composites. *J. Am. Ceram. Soc.*, 1983, **66**(8), C-125-C-127.
- [8] Descamps, P., Sakaguchi, S., Poorteman, M., Cambier, F. High-temperature characterization of reaction-sintered mullite-zirconia composites. *J. Am. Ceram. Soc.*, 1991, **74**(10), 2476–2481.
- [9] Scudeller, L. A. M., Longo, E., Varela, J. A. Potassium vapor attack in refractories of the alumina–silica system. *J. Am. Ceram. Soc.*, 1990, **73**(5), 1413–1416.
- [10] WHO. IARC, monographs on the evaluation of carcinogenic risks to humans: man-made vitreous fibres. Lyon, IARC Press, 2002, **81**, 41-338.
- [11] WHO. IARC, Monographs on the evaluation of carcinogenic risks to humans: man-made mineral fibres and radon. Lyon, IARC Press, 1988, **43**, 33-171.
- [12] Modarresifar, F., Bingham, P. A., Jubb, G. A. Thermal conductivity of refractory glass fibres. *J. Therm. Anal. Calorim.*, 2016, **125**(1), 35–44.
- [13] Wainwright, R., Jubb, G., Fadiora, F. Inorganic Fibre Compositions. *U.S. Patent # 9,944,552 B2*. 2018.
- [14] Schairer, J. F., Bowen, N. L. The system  $K_2O-Al_2O_3-SiO_2$ . *Am. J. Sci.*, 1955, **253**(12), 681–746.
- [15] Osborn, E. F., Muan, A. Phase equilibrium diagrams for ceramists. Plate 5. The system  $K_2O-Al_2O_3-SiO_2$ . Columbus OH, 1960.
- [16] Christopoulou, G., Modarresifar, F., Allsopp, B. L., Jones, A. H., Bingham, P. A. Nonisothermal crystallization kinetics and stability of leucite and kalsilite from  $K_2O-Al_2O_3-SiO_2$  glasses. *J. Am. Ceram. Soc.*, 2019, **102**(1), 508–523.
- [17] Takei, T., Kameshima, Y., Yasumori, A., Okada, K. Crystallization kinetics of mullite from  $Al_2O_3-SiO_2$  glasses under non-isothermal conditions. *J. Eur. Ceram. Soc.*, 2001, **21**(14), 2487–2493.
- [18] Cook, L. P., Roth, R. S., Parker, H. S., Negas, T. The system  $K_2O-Al_2O_3-SiO_2$ ; Part 1, Phases on the  $KAlSiO_4-KAlO_2$  join. *Am. Mineral.*, 1977, **62**(11–12), 1180–1190.
- [19] Höland, W., Frank, M., Rheinberger, V. Surface crystallization of leucite in glasses. *J. Non-Cryst. Solids.*, 1995, **180**(2), 292–307.

- [20] Sadik, C., Amrani, I. E., Albizane A. Recent advances in silica-alumina refractory: A review. *J. Asian Ceram. Soc.*, 2014, **2**(2), 83–96.
- [21] Cattell, M. J., Chadwick, T. C., Knowles, J. C., Clarke, R. L. The crystallization of an aluminosilicate glass in the  $K_2O-Al_2O_3-SiO_2$  system. *Dent. Mater.*, 2005, **21**(9), 811–822.
- [22] Cattell, M. J., Chadwick, T. C., Knowles, J. C., Clarke, R. L., Samarawickrama, DYD. The nucleation and crystallization of fine-grained leucite glass-ceramics for dental applications. *Dent. Mater.*, 2006, **22**(10), 925–933.
- [23] Sacks, M. D., Bozkurt, N., Scheiffele, G. W. Fabrication of mullite and mullite-matrix composites by transient viscous sintering of composite powders. *J. Am. Ceram. Soc.*, 1991, **74**(10), 2428–2437.
- [24] Yazhenskikh, E., Hack, K., Müller, M. Critical thermodynamic evaluation of oxide systems relevant to fuel ashes and slags, Part 5: Potassium oxide–alumina–silica. *Calphad.*, 2011, **35**(1), 6–19.
- [25] Holand, W., Beall, G. H. Glass Ceramic Technology. 2<sup>nd</sup> Ed, Hoboken, John Wiley & Sons New Jersey, 2012.
- [26] Karell, R., Chromčíková, M., Liška, M. Structure and properties of selected zirconia silicate glasses. *Adv. Mat. Res.*, 2008, **39–40**, 173–176.
- [27] McMillan, P. W. Glass-ceramics, Academic Press, London, 1979.
- [28] Farges, F., Ponader, C. W., Brown, G.E. Structural environments of incompatible elements in silicate glass/melt systems: I. Zirconium at trace levels. *Geochim. Cosmochim. Acta.*, 1991, **55**(6), 1563–1574.
- [29] Vogel, W. Glass Chemistry (2<sup>nd</sup> Ed), Springer-Verlag, London, 1994.
- [30] Ficheux, M., Burov, E., Cormier, L., Gouillart, E., Trcera, N. Influence of zirconium on cation mobilities in  $Na_2O-CaO-Al_2O_3-SiO_2$  melts: A multicomponent diffusion and XANES study. *Geochim. Cosmochim. Acta.*, 2020, **270**, 394–408.
- [31] Kissinger, H. E. Reaction Kinetics in differential thermal analysis. *Anal. Chem.*, 1957, **29**(11), 1702–1706.
- [32] Hu, L., Jiang, Z., A new criterion for crystallization of glass, *J. Chin. Ceram. Soc.*, 1990, **18**(4), 315–321.
- [33] Doremus, R. H., Glass Science (2<sup>nd</sup> Ed.), John Wiley & Sons, New York, 1994.
- [34] Kovarik, L., Bowden, M., Andersen, A., Jaegers, N. R., Washton, N., Szanyi, J. Quantification of High-Temperature Transition  $Al_2O_3$  and Their Phase Transformations. *Angewandte Chemie.*, 2020, **132**, 21903–21911.
- [35] Kim, D. G., Konar, B., Jung, I. H. Thermodynamic optimization of the  $K_2O-Al_2O_3-SiO_2$  system. *Ceram. Int.*, 2018, **44**(14), 16712–16724.
- [36] Chauruka, S., Hassanpour, A., Brydson, R., Roberts, K., Ghadiri, M., Stitt, H. Effect of mill type on the size reduction and phase transformation of gamma alumina. *Chem. Eng. Sci.*, 2015, **134**(29), 774–783.
- [37] Inoue, H., Nagashima, Y., Yasui, I. Non-isothermal crystallization mechanism in  $ZrF_4-BaF_2-RF_3$  (R=Al, La) Glasses. *J. Ceram. Assoc. Jpn.*, 1987, **95**(1105), 845–853.
- [38] Zhao, X., Sakka, S. Glass formation and crystallization in alkali-containing fluoride glasses. *J. Non-Cryst. Solids.*, 1987, **95–96**, 487–494.
- [39] Kozmidis-Petrovic, A., Šesták, J. Forty years of the Hrubý glass-forming

coefficient via DTA when comparing other criteria in relation to the glass stability and vitrification ability. *J. Therm. Anal. Calorim.*, 2012, **110**(2), 997–1004.

[40] Ray, C. S., Reis, S. T., Brow, R. K., Höland, W., Rheinberger, V. A new DTA method for measuring critical cooling rate for glass formation. *J. Non-Cryst. Solids.*, 2005, **351**(16), 1350–1358.

[41] Yue, Y-Z. Characteristic temperatures of enthalpy relaxation in glass. *J. Non-Cryst. Solids.*, 2008, **354**(12), 1112–1118.

[42] Polyakova, I. G. The criterion for the crystallization ability assessment as applied to borate glass powders and monoliths. *Entropy.*, 2019, **21**(10), 994.

[43] Uhlmann, D. R. Glass formation. *J. Non-Cryst. Solids.*, 1977, **25**(1), 42–85.

[44] Uhlmann, D. R. A kinetic treatment of glass formation. *J. Non-Cryst. Solids.*, 1972, **7**(4), 337–348.

[45] Weinberg, M. C., Uhlmann, D. R., Zanotto, E. D. “Nose Method” of calculating critical cooling rates for glass formation. *J. Am. Ceram. Soc.*, 1989, **72**(11), 2054–2058.

[46] Hrubý, A. Evaluation of glass-forming tendency by means of DTA. *Czech. J. Phys. B.*, 1972, **22**(11), 1187–1193.

[47] Kauzmann, W. The nature of the glassy state and the behavior of liquids at low temperatures. *Chem. Rev.*, 1948, **43**(2), 219–256.

[48] Turnbull, D. Under what conditions can a glass be formed? *Contemp. Phys.*, 1969, **10**(5), 473–488.

[49] Fokin, V. M., Nascimento, M. L. F., Zanotto, E. D. Correlation between maximum crystal growth rate and glass transition temperature of silicate glasses. *J. Non-Cryst. Solids.*, 2005, **351**(10), 789–794.

[50] Nascimento, M. L. F., Souza, L. A., Ferreira, E. B., Zanotto, E. D. Can glass stability parameters infer glass forming ability? *J. Non-Cryst. Solids.*, 2005, **351**(40), 3296–3308.

[51] Lu, Z. P., Liu, C. T. A new approach to understanding and measuring glass formation in bulk amorphous materials. *Intermetall.*, 2004, **12**(10), 1035–1043.

[52] Weinberg, M. C. Glass-formation and crystallization kinetics. *Thermochim. Acta.*, 1996, **280–281**, 63–71.

[53] Lu, Z. P., Liu, C. T. A new glass-forming ability criterion for bulk metallic glasses. *Acta Materialia.*, 2002, **50**(13), 3501–3512.

[54] Lu, Z. P., Liu, C. T. Glass formation criterion for various glass-forming systems. *Phys. Rev. Lett.*, 2003, **91**(11), 115505.

[55] Jiusti, J., Cassar, D. R., Zanotto, E. D. Which glass stability parameters can assess the glass-forming ability of oxide systems? *Int. J. Appl. Glass Sci.*, 2020, **00**, 1–10.

[56] Karell, R., Kraxner, J., Chromcikova, M. Properties of selected zirconia containing silicate glasses. *Ceram.-Silikaty*, 2006, **50**(2), 78–82.

Table 1. Nominal glass compositions in the K<sub>2</sub>O-Al<sub>2</sub>O<sub>3</sub>-SiO<sub>2</sub> mixed with/without ZrO<sub>2</sub> (wt.%).

	KAS1	KAS1-Z	KAS2	KAS2-Z
Al <sub>2</sub> O <sub>3</sub>	38.8	36.1	45.8	41.6
K <sub>2</sub> O	28.0	26.0	15.1	13.9
SiO <sub>2</sub>	33.2	30.9	39.1	37.3
ZrO <sub>2</sub>	0.0	7.0	0.0	7.2

Table 2. Raw materials used for glass production.

Raw material	Purity	Supplier
Al <sub>2</sub> O <sub>3</sub>	>99.0%	Richard Baker Harrison Ltd.
K <sub>2</sub> CO <sub>3</sub>	>99.5%	Norkem Ltd.
SiO <sub>2</sub>	>99.6%	Sibelco UK Ltd.
ZrSiO <sub>4</sub>	>99.0%	Richards Bay Minerals Ltd.

Table 3. XRF-analyzed compositions for all glass samples (wt. %)

	KAS1	KAS1-Z	KAS2	KAS2-Z
Al <sub>2</sub> O <sub>3</sub>	37.4	35.1	45.7	41.8
K <sub>2</sub> O	27.9	25.7	14.5	13.8
SiO <sub>2</sub>	34.7	31.7	39.8	37.3
ZrO <sub>2</sub>	0.0	7.5	0.0	7.1

\*Uncertainties associated with the XRF analyses are estimated at ±2% of measured concentrations.

Table 4. a. Crystallization activation energy for different glass samples.

Glass	$E_a$ for Peak 1 <sup>†</sup> (kJ/mol)	$E_a$ for Peak 2 <sup>†</sup> (kJ/mol)	$E_a$ for Peak 3 <sup>†</sup> (kJ/mol)
KAS1	-	492.0 / KAlSiO <sub>4</sub>	-
KAS1-Z	559.9 / ZrO <sub>2</sub>	494.0 / KAlSiO <sub>4</sub>	-
KAS2	-	722.8 / $\gamma$ -Al <sub>2</sub> O <sub>3</sub>	488.6 / KAlSi <sub>2</sub> O <sub>6</sub>
KAS2-Z	1018.9 / ZrO <sub>2</sub>	529.7 / $\gamma$ -Al <sub>2</sub> O <sub>3</sub>	496.0 / KAlSi <sub>2</sub> O <sub>6</sub>

<sup>†</sup> Peak number is according to the order of appearance, with increasing temperature, of exothermic peaks from DSC.

Table 4. b. Average shape factor ( $n$ ) for different crystallisation events.

Glass	Shape factor for Peak 1 <sup>†</sup> ( $n \pm 0.1$ )	Shape factor for Peak 2 <sup>†</sup> ( $n \pm 0.1$ )	Shape factor for Peak 3 <sup>†</sup> ( $n \pm 0.1$ )
KAS1	\	3.6/ KAlSiO <sub>4</sub>	\
KAS1-Z	1.4/ ZrO <sub>2</sub>	2.3/ KAlSiO <sub>4</sub>	\
KAS2	\	1.6/ $\gamma$ -Al <sub>2</sub> O <sub>3</sub>	4.2/ KAlSi <sub>2</sub> O <sub>6</sub>
KAS2-Z	2.1/ ZrO <sub>2</sub>	1.3/ $\gamma$ -Al <sub>2</sub> O <sub>3</sub>	3.5/ KAlSi <sub>2</sub> O <sub>6</sub>

<sup>†</sup> Peak number is defined according to order of occurrence, with increasing temperature, of exothermic peaks from DSC.

**Table 5** Characteristic temperatures for glass stability (GS) parameter derivation.

DSC, 20°C/min (±2°C)	Sample KAS1		Sample KAS1-Z		Sample KAS2		Sample KAS2-Z	
	Temp./ °C	Phase	Temp./°C	Phase	Temp./ °C	Phase	Temp./°C	Phase
T <sub>g</sub> (°C)	831	/	888	/	918	/	923	/
†T <sub>x1</sub> /T <sub>c1</sub> (°C)	/	/	942/998	ZrO <sub>2</sub>	/	/	972/987	ZrO <sub>2</sub>
T <sub>x2</sub> /T <sub>c2</sub> ( <sup>o</sup> C)	1087/1 105	KAlSiO <sub>4</sub>	1092/1 112	KAlSiO <sub>4</sub>	994/102 2	γ-Al <sub>2</sub> O <sub>3</sub>	977/1025	γ-Al <sub>2</sub> O <sub>3</sub>
T <sub>x3</sub> /T <sub>c3</sub> ( <sup>o</sup> C)	/	/	/	/	1313/13 38	KAlSi <sub>2</sub> O <sub>6</sub>	1293/1322	KAlSi <sub>2</sub> O 6
T <sub>m</sub> (°C)	1800‡	/	Unknown	/	1760‡	/	Unknown	

† T<sub>x</sub> denotes the onset crystallization temperature and T<sub>c</sub> denotes the peak crystallization temperature. The number indicates the thermal peaks in order from low to high temperature.

‡ Melting temperatures were interpreted from liquidus surfaces in the phase diagram calculated by Yazhenshikh *et al.* [24]

Table 6 Glass stability (GS) criteria based on characteristic temperatures.

GS parameter	Source	Developers:	Sample KAS1	Sample KAS1-Z		Sample KAS2		Sample KAS2-Z		
			KAlSiO <sub>4</sub> (1105°C)	ZrO <sub>2</sub> (998 °C)	KAlSiO <sub>4</sub> (1112°C)	γ-Al <sub>2</sub> O <sub>3</sub> (1022°C)	KAlSi <sub>2</sub> O <sub>6</sub> (1338°C)	ZrO <sub>2</sub> (987 °C)	γ-Al <sub>2</sub> O <sub>3</sub> (1025°C)	KAlSi <sub>2</sub> O <sub>6</sub> (1322 °C)
$K_H = (T_x - T_g) / (T_m - T_x)$		Hrubý [46]	0.360	<0.063	<0.288	0.099	0.884	<0.062	<0.069	<0.792
$K_W = (T_c - T_g) / T_m$	Characteristic temperature	Weinberg [52]	0.152	<0.061	<0.124	0.059	0.239	<0.036	<0.058	<0.227
$K_{LL} = T_c / (T_g + T_m)$		Lu & Liu [53,54]	0.420	<0.371	<0.414	0.382	0.500	<0.368	<0.382	<0.493
$k_p = \gamma \exp(-E_a/RT_p)$	Activation energy	Hu [32]	0.32	0.48	0.32	0.50	0.23	0.47	0.44	0.22

## Figures captions:

**Figure 1.** Refractory compositions (on the K<sub>2</sub>O-R dotted line) from Scudeller *et al.* [9]

(S=Silica; M= Mullite; L, L2, L3=Liquid; PF=Potash Feldspar; Le=Leucite; C=Corundum; K=Kaliophilite.)

Reproduced with permission of the Journal of the American Ceramic Society, license # 4860380913652.

**Figure 2.** K<sub>2</sub>O-Al<sub>2</sub>O<sub>3</sub>-SiO<sub>2</sub> ternary phase diagram experimentally studied by Schairer and Bowen [14] and revised and redrawn by Osborn and Muan [15]Reproduced from phase equilibria diagrams online database (NIST standard Reference Database 31, Figure 00407), with permission of The American Ceramic Society.

**Figure 3.** Isothermal section in the K<sub>2</sub>O-Al<sub>2</sub>O<sub>3</sub>-SiO<sub>2</sub> diagram at 1200°C from Kingery *et al.* [1] (Note: KAS<sub>2</sub> is the composition K<sub>2</sub>O·Al<sub>2</sub>O<sub>3</sub>·2SiO<sub>2</sub>). Reproduced with permission of Wiley publishers, license # 4860380753214.

**Figure 4.** Compositions of samples KAS1 and KAS2 illustrated on a K<sub>2</sub>O-Al<sub>2</sub>O<sub>3</sub>-SiO<sub>2</sub> phase diagram[24]. Reproduced with permission of Calphad, license # 4860380335995.

**Figure 5. a.** DSC curves for KAS1 glass in different heating rates (from 5°C/min to 40°C/min).

**Figure 5. b.** DSC curves for KAS1-Z glass in different heating rates (from 5°C/min to 40°C/min).

**Figure 5. c.** DSC curves for KAS2 glass in different heating rates (from 5°C/min to 40°C/min).

**Figure 5. d.** DSC curves for KAS2-Z glass in different heating rates (from 5°C/min to 40°C/min).

**Figure 6.** XRD patterns for as prepared glass samples of KAS1, KAS2, KAS1-Z and KAS2-Z.

**Figure 7. a.** XRD pattern for sample KAS2 heat treated at 1020°C for 10 mins.

**Figure 7. b.** XRD pattern for sample KAS2 heat treated at 1330°C for 10 mins.

**Figure 8. a.** XRD patterns for samples KAS1 heat treated at 1250°C from 5 minutes to 24 hours.

**Figure 8. b.** XRD patterns for samples KAS1-Z heat treated at 1250°C from 5 minutes to 24 hours.

**Figure 8. c.** XRD patterns for samples KAS2 heat treated at 1250°C from 5 minutes to 24 hours.

**Figure 8. d.** XRD patterns for samples KAS2-Z heat treated at 1250°C from 5 minutes to 24 hours.

**Figure 9. a.** Kissinger plots for non-isothermal crystallization of KAlSiO<sub>4</sub> in sample KAS1.

**Figure 9. b.** Kissinger plots for non-isothermal crystallization of ZrO<sub>2</sub> at ~1000°C and KAlSiO<sub>4</sub> at ~1100 °C in sample KAS1-Z..

**Figure 9. c.** Kissinger plots for non-isothermal crystallization of  $\gamma$ -Al<sub>2</sub>O<sub>3</sub> at ~1000 °C and KAlSi<sub>2</sub>O<sub>6</sub> at ~1300 °C in sample KAS2.

**Figure 9. d.** Kissinger plots for non-isothermal crystallization of ZrO<sub>2</sub> <1000°C,  $\gamma$ -Al<sub>2</sub>O<sub>3</sub> at ~1000°C and KAlSi<sub>2</sub>O<sub>6</sub> at ~1300 °C in sample KAS2-Z.